



ORIGINAL RESEARCH COMMUNICATION

Structure and Function of Redox-Sensitive Superfolder Green Fluorescent Protein Variant

Kim C. Heimsch,¹ Christoph G.W. Gertzen,^{2,3} Anna Katharina Schuh,¹ Thomas Nietzel,⁴ Stefan Rahlfs,¹ Jude M. Przyborski,¹ Holger Gohlke,^{2,5} Markus Schwarzländer,⁴ Katja Becker,¹ and Karin Fritz-Wolf^{1,6}

Abstract

Aims: Genetically encoded green fluorescent protein (GFP)-based redox biosensors are widely used to monitor specific and dynamic redox processes in living cells. Over the last few years, various biosensors for a variety of applications were engineered and enhanced to match the organism and cellular environments, which should be investigated. In this context, the unicellular intraerythrocytic parasite *Plasmodium*, the causative agent of malaria, represents a challenge, as the small size of the organism results in weak fluorescence signals that complicate precise measurements, especially for cell compartment-specific observations. To address this, we have functionally and structurally characterized an enhanced redox biosensor superfolder roGFP2 (sfroGFP2).

Results: SfroGFP2 retains roGFP2-like behavior, yet with improved fluorescence intensity (FI) *in cellulo*. SfroGFP2-based redox biosensors are pH insensitive in a physiological pH range and show midpoint potentials comparable with roGFP2-based redox biosensors. Using crystallography and rigidity theory, we identified the superfolding mutations as being responsible for improved structural stability of the biosensor in a redox-sensitive environment, thus explaining the improved FI *in cellulo*.

Innovation: This work provides insight into the structure and function of GFP-based redox biosensors. It describes an improved redox biosensor (sfroGFP2) suitable for measuring oxidizing effects within small cells where applicability of other redox sensor variants is limited.

Conclusion: Improved structural stability of sfroGFP2 gives rise to increased FI *in cellulo*. Fusion to hGrx1 (human glutaredoxin-1) provides the hitherto most suitable biosensor for measuring oxidizing effects in *Plasmodium*. This sensor is of major interest for studying glutathione redox changes in small cells, as well as subcellular compartments in general. *Antioxid. Redox Signal.* 37, 1–18.

¹Biochemistry and Molecular Biology, Interdisciplinary Research Center, Justus Liebig University Giessen, Giessen, Germany.

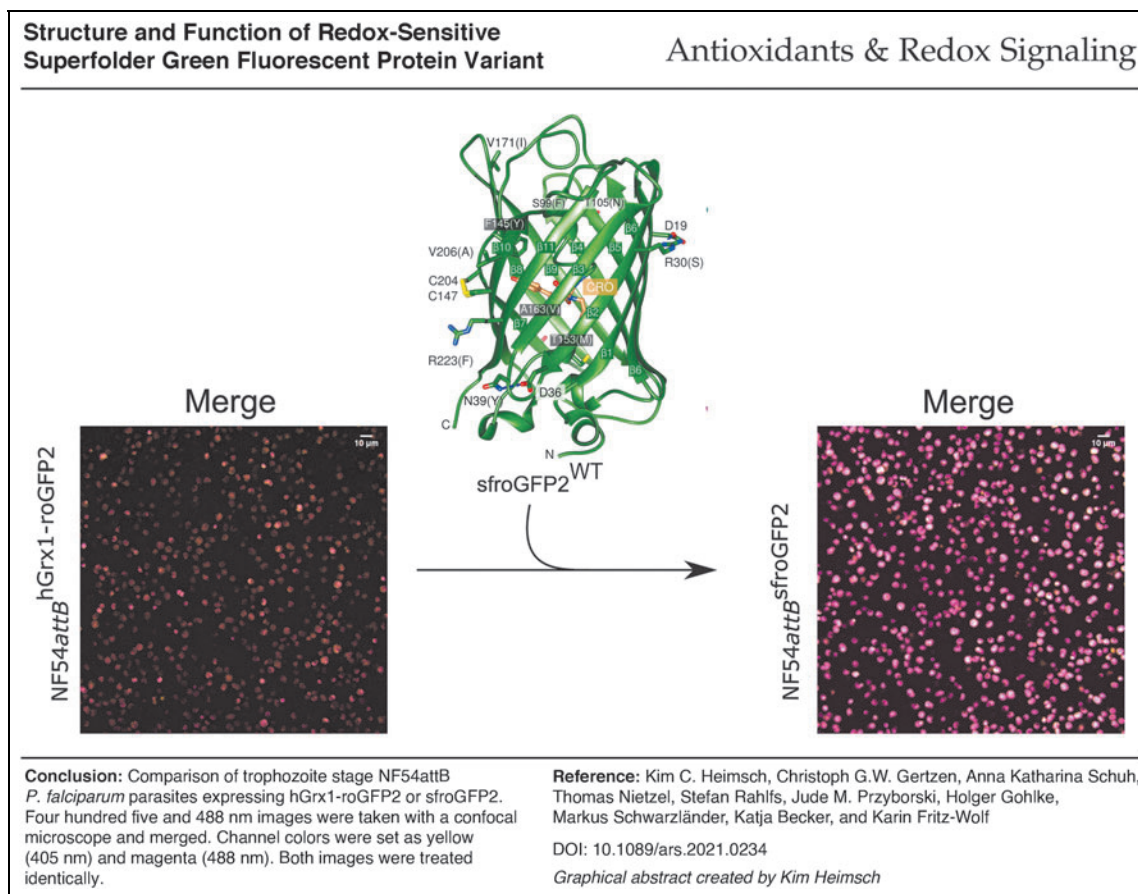
²Institute for Pharmaceutical and Medicinal Chemistry, Heinrich Heine University Düsseldorf, Düsseldorf, Germany.

³Center for Structural Studies (CSS), Heinrich Heine University Düsseldorf, Düsseldorf, Germany.

⁴Institute of Plant Biology and Biotechnology, University of Münster, Münster, Germany.

⁵John von Neumann Institute of Computing (NIC), Jülich Supercomputing Centre (JSC), Institute of Biological Information Processing (IBI-7: Structural Biochemistry), and Institute of Bio- and Geosciences (IBG-4: Bioinformatics), Forschungszentrum Jülich GmbH, Jülich, Germany.

⁶Max-Planck Institute of Medical Research, Heidelberg, Germany.



Keywords: GFP, genetically encoded biosensors, X-ray crystal structure, molecular dynamics simulation, redox regulation, *Plasmodium falciparum*

Introduction

THE GREEN FLUORESCENT PROTEIN (GFP) from the jellyfish *Aequorea victoria* (51, 67) possesses a *p*-hydroxybenzylidene-imidazolidinone chromophore, which

Innovation

The small size of *Plasmodium* parasites and their lifestyle, including their presence in highly pigmented erythrocytes, makes fluorescence-based measurement difficult. This is further complicated when measurements in subcellular compartments are to be performed. Generating a redox biosensor that shows improved fluorescence intensity *in cellulo* considerably enhances the quality of the measurement method (graphical abstract). The deep structural and functional insight into the sensor properties gained by this study suggests that specific mutations can significantly improve the stability of a biosensor and thereby its *in cellulo* performance. This study provides a blueprint for rational optimization of biosensors to match specific biological requirements.

is formed upon internal cyclization and oxidation of the three amino acids (AAs) Ser, Tyr, and Gly (19, 41). Dependent on the protonation/ionization state of the chromophore, GFP has two excitation maxima, at 395 and 475 nm, both giving rise to emission with a maximum at 508 nm (3, 67). Due to the β -barrel structure of GFP, the chromophore is largely shielded from the surrounding solvents (3). Over the years, the spectral properties of the original wild-type (WT) *avGFP* (*Aequorea victoria* GFP) have been optimized through protein engineering. In nature, WT *avGFP* associates aequorin, involving hydrophobic interaction of the protein surfaces; absence of aequorin can cause aggregation.

The so-called cycle three mutations (F99S, M153T, and V163A) result in more hydrophilic residues, reduce aggregation, and improve chromophore activation (8). Including these resulted in a GFP version with the generation of a stronger fluorescence signal; however, excitation maxima remained unchanged (8). Additional mutations (F64L, S65T) in combination lead to an increase in fluorescence intensity (FI) compared with WT *avGFP* (7, 70). Pédelacq *et al.* added further mutations (S30R, Y39N, N105T, Y145F, I171V, and A206V) to generate superfolder (sf) GFP. Those mutations lead to improved thermodynamic stability, faster folding, and decreased folding interference (45).

Besides using GFP as a fluorescence reporter in a wide range of cell biological applications, it has been utilized to generate a redox-sensitive biosensor that allows ratiometric, real-time measurements in living cells. By inserting cysteine pairs into juxtaposed β -strands of the GFP barrel surface, spectral changes of the chromophore are dependent on alterations in redox potential of redox couples that are able to react and equilibrate with the thiol/disulfide redox switch (18). The two excitation maxima of roGFP (reduction/oxidation-sensitive green fluorescent protein) are shifted to ~ 400 and 490 nm (18).

We have previously used GFP-based redox biosensors to study oxidizing effects within *Plasmodium falciparum* parasites (32, 64), which replicate within mature human red blood cells. Malaria parasites encounter oxidative challenge, for example, due to the parasite's high metabolic rate, from products of red blood cell hemoglobin digestion during the intraerythrocytic life cycle and the immune responses of the host (28). Furthermore, it is known that some antimalarials mediate their effect at least partially by increasing the production rates of reactive oxygen species and of other free radicals (33). Therefore, studying changes in the redox metabolism of *Plasmodium* parasites is of considerable interest to understand the mode of action of new antimalarials, as well as resistance mechanisms.

The small size of *Plasmodium* parasites ($2\text{--}5\ \mu\text{m}$ in the asexual erythrocytic stages usually studied) has been technically challenging for fluorimetry and imaging approaches, as well as the high background pigmentation of the host cell. Membrane-bound subcompartments of the parasites (apicoplast, mitochondrion, parasitophorous vacuole) are even smaller, further complicating precise measurement of cellular parameters. Fluorescence signals of commonly used redox biosensors regularly result in comparatively worse signal-to-noise ratios, further complicating the situation. This is even more the case for measurements in subcellular compartments with small volume such as the mitochondrial matrix.

In previous work, the two cysteines S147C and Q204C, as well as the F223R mutation from roTurbo (13), were included in sfGFP, resulting in sfroGFP2 (superfolder reduction/oxidation-sensitive GFP2, sfroGFP2^{WT}), which showed strongly increased FI *in cellulo* (graphical abstract) (64).

In this study, we characterized sfroGFP2 to assess its functionality in *Plasmodium* parasites. We presented a X-ray crystal structure resolved to $1.1\ \text{\AA}$ and used this as a basis to examine the structural stability of the protein further. Structural stability can be probed by modeling the structures as constraint networks, where atoms as nodes are connected by constraints due to covalent and noncovalent bonds, and *via* subsequent analysis based on a rigidity theory (24, 49, 50, 57). We tested the hypothesis that the improved fluorescence and robustness of sfroGFP2^{WT} may be related to a higher structural stability of this variant (46).

To gain empirical insights into the relative contribution of specific residues to the modified structural and functional properties of sfroGFP2^{WT}, we removed specific superfolder mutations, namely S30R, Y39N, and F223R. Based on the crystal structure of sfroGFP2^{WT}, it is very unlikely that both sf mutations Y147F and I171V influence the structure to any major extent. Furthermore, as already stated by Pédelacq *et al.*, the N105T side chain does not affect the orientation of the adjacent residue side chains. In sfGFP, the mutation

A206V comes into close contact with the phenyl group of F223 (45). However, since the AA at position 223 points toward the solvent phase, we did not assume an impact to the structural stability. We have therefore focused our examinations on both sf mutations S30R and Y39N, and did not focus on any of the other sf mutations, since we did not assume major effects to the structure of the sensor.

Gutscher *et al.* fused roGFP to human glutaredoxin-1 (hGrx1), thereby generating a proximity-based biosensor that specifically equilibrates with the glutathione couple, thus overcoming uncertainties about the *in vivo* specificity of the free roGFP biosensor, as well as slow responsiveness (17, 18). Taking our lead from this, we have here fused sfroGFP2^{WT} to hGrx1, combining the advantages of a specific and fast responding biosensor resulting from hGrx1-fusion with the increased FI of sfroGFP2^{WT}.

Results

The improved redox biosensor sfroGFP2^{WT} shares 94% sequence identity with *av*GFP. It contains all roGFP2 substitutions plus the sf mutations (45) (Fig. 1A), as well as F223R (13). This sensor was recently published by our research group and showed favorable properties as compared with the commonly used roGFP2 variant when used *in cellulo* (64).

To determine whether the two specific sf mutations S30R and Y39N are involved in increasing the stability of sfroGFP2^{WT} compared with roGFP2, we reversed these two mutations, as well as F223R, one at a time. We investigated the three reversion mutants (mutants are called throughout the article as follows: sfroGFP2^{R30S}, sfroGFP2^{N39Y}, and sfroGFP2^{R223F}), as well as sfroGFP2^{WT} and the fusion sensor hGrx1-sfroGFP2, in comparison with roGFP2 and hGrx1-roGFP2, by using a set of complementary methods, we (i) determined and analyzed the crystal structures of sfroGFP2^{WT}, sfroGFP2^{R30S}, and sfroGFP2^{N39Y}; (ii) performed rigidity analysis for sfroGFP2^{WT} and a set of different models based on it; and (iii) assessed the spectral and functional properties of all roGFP2- and sfroGFP2^{WT}-based biosensors.

Crystal structure analysis

We obtained orthorhombic and monoclinic crystals of sfroGFP2^{WT}. The sfroGFP2^{WT} protein crystallizes in space group $P2_12_12_1$ and contains one monomer in the asymmetric unit. SfroGFP2^{R30S} and sfroGFP2^{N39Y} obey $P2_1$ symmetry, with two or four monomers in the asymmetric unit, respectively. The sfroGFP2^{WT} crystal diffracted to a resolution of $1.1\ \text{\AA}$, and the mutants sfroGFP2^{R30S} and sfroGFP2^{N39Y} to $1.4\ \text{\AA}$ and $2.0\ \text{\AA}$, respectively. All structures were solved *via* molecular replacement. Data collection and refinement statistics of all datasets are summarized in Table 1.

The sfroGFP2^{WT} monomer (238 AA) adopts the canonical GFP fold, which comprises an 11-stranded β -barrel with an inner α -helix, containing the covalently bound chromophore 4-(*p*-hydroxybenzylidene)imidazolidine-5-one (Fig. 1A). In our structures, the two cysteines C147 and C204, which are able to respond to the ambient redox environments and fundamental for the use of roGFP variants as redox sensors, form a disulfide bridge.

All sf mutations are located on the surface of the barrel. Two of the sf mutations (S30R, Y39N) are of particular

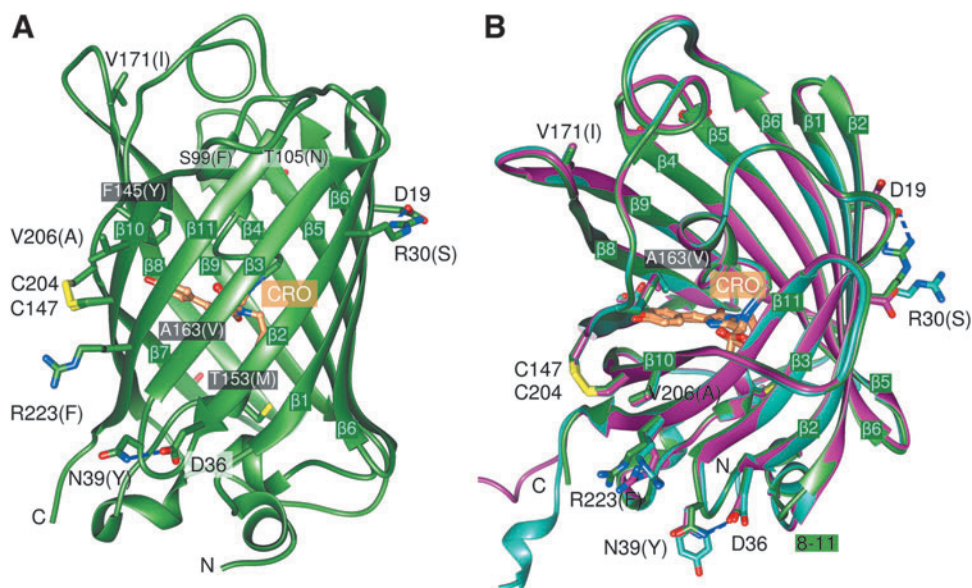


FIG. 1. X-ray crystal structure analysis of sfroGFP2^{WT}, sfroGFP2^{R30S}, and sfroGFP2^{N39Y}. (A) Model of sfroGFP2^{WT} based on X-ray crystal structure analysis. The protein crystal diffracted to a resolution of 1.1 Å. The structure was solved *via* molecular replacement. The two cysteines C147 and C204 form a disulfide bridge (represented in yellow). The chromophore is shown in orange. All sf mutations and both the cysteine mutations, which are elementary for the usage of GFP as a redox sensor, are labeled. The *letter in brackets* indicates the AA in the original roGFP2. Furthermore, the N and C-termini are labeled. (B) Structural comparison between sfroGFP2^{WT} (green), sfroGFP2^{R30S} (magenta), and sfroGFP2^{N39Y} (turquoise). The sfroGFP2^{R30S} and sfroGFP2^{N39Y} crystals diffracted to a resolution of 1.4 Å and 2.0 Å, respectively. All structures were solved *via* molecular replacement. The individual β -strands are labeled. The main structural differences between the three variants occur at the N-terminus and in the loop region 8–11. AA, amino acid; CRO, chromophore; GFP, green fluorescent protein; sf, superfolder.

interest because they give rise to novel interactions between neighboring β -strands. In sfroGFP2^{WT}, residues R30 and N39 form hydrogen bonds to D19 and D36, respectively (Fig. 1A); these interactions do not occur in roGFP2. For the F223R mutation, we did not expect any effect on the X-ray structure because R223 points toward the solvent phase (Fig. 1A) and is unlikely to interact with other AA. For this reason, we focused our efforts on the sfroGFP2^{R30S} and sfroGFP2^{N39Y} variants.

As mentioned above, the sfroGFP2^{WT}, sfroGFP2^{R30S}, and sfroGFP2^{N39Y} structures contain one, two, and four monomers of sfroGFP2 in the asymmetric unit, respectively. The 7 monomers are similar, with root-mean-square deviation values of 0.3 Å to 0.8 Å with 228 C α atoms. Differences occur at the N-terminus and in the location of a surface loop (8–11) (Fig. 1B). However, this region is involved in monomer-monomer interactions of the mutants and seems unlikely to be relevant for the stability properties of sfroGFP2^{WT}.

In the sfroGFP2^{WT} structure, there is an ion pair network in the vicinity of R30 that involves four neighboring strands of the β -barrel. R30, located centrally on a β -strand (β 2 Fig. 2), interacts with D19 from the adjacent strand (β 1). The next strand (β 6) is connected to β 1 by a bond between E17 (β 1) and R122 (β 6). Moreover, R122 forms a salt bridge to E115 (β 5). Furthermore, E111 (β 5) and K113 (β 5) are connected by a bond. Therefore, the strands β 1, β 2, β 5, and β 6 are connected *via* a network of ionic interactions.

Superimposition of the four monomers from the sfroGFP2^{N39Y} structure reveals that the side chain of R30 (β 2) adopts different conformations in the subunits, thereby interacting with E32 (β 2) or E17 (β 1). The interaction

between R122 (β 6) and E115 (β 5) is present in all four subunits, but only in two sfroGFP2^{N39Y} monomers (A, B) does R122 (β 6) interact with E17 (β 1). K113 also adopts several conformations, but only in one subunit (D) does it interact with another residue (E115, β 5) (Fig. 2).

Due to the reversed R30S (β 2) mutation in sfroGFP2^{R30S}, the much smaller side chain of S30 is not able to interact with residues D19 (β 1) or E32 (β 2) instead, S30 interacts with E17 (β 1) through a hydrogen bond. Due to the high strength of this interaction, the E17 side chain adopts a completely different conformation from that seen in the sfroGFP2^{WT}—or the four sfroGFP2^{N39Y}—structures. Consequently, R122 (β 6) is no longer able to connect strands β 1 and β 6 (Fig. 2).

In the sfroGFP2^{WT} structure, N39 interacts with D36 through a hydrogen bond (Fig. 1A); in the sfroGFP2^{N39Y} structure, Y39 points into the solvent (Fig. 1B). Of interest is the small apparent shift of the chromophore within the barrel by \sim 0.2 Å in the sfroGFP2^{R30S} and 0.3 Å in the sfroGFP2^{N39Y} structures. However, since the coordinate errors are almost as large, the shift cannot be resolved with any certainty.

Larger differences are seen in the network of ionic interactions within the three variants. The most complex ion network is formed in the sfroGFP2^{WT}, which therefore presumably contributes to a higher structural stability of the protein.

Rigidity analysis

To obtain structural stability information as a direct link to the functional properties of the protein, we next used the

TABLE 1. CRYSTALLOGRAPHIC STATISTICS

	<i>sfroGFP2</i> ^{WT}	<i>sfroGFP2</i> ^{R30S}	<i>sfroGFP2</i> ^{N39Y}
Space group	P2 ₁ 2 ₁ 2 ₁	P12 ₁ 1	P12 ₁ 1
Unit cell parameters			
a, b, c, Å	36.87, 47.37, 117.74	51.11, 68.92, 68.45	91.85, 51.29, 101.46
α, β, γ, °	90, 90, 90	90, 104.038, 90	90, 102.282, 90
Data collection			
Beamline	SLS beam line X10SA	SLS beam line X10SA	SLS beam line X10SA
Temperature, K	100	100	100
Wavelength, Å	1	0.9998	0.9998
Resolution range	19.85–1.05 (1.09–1.05)	45.35–1.35 (1.4–1.35)	47.92–2.0 (2.07–2.0)
Wilson B-factor	8.9	17.2	26.7
Total reflections	391,518 (10,387)	483,809 (19,241)	144,797 (15,047)
Unique reflections	89,058 (4957)	95,798 (6718)	59,713 (5842)
Multiplicity	4.4 (2.1)	5.1 (2.9)	2.4 (2.6)
Completeness, %	91.7 (51.7)	94.8 (66.9)	94.5 (93.0)
Mean <i>I</i> /σ, <i>I</i>	16.2 (2.6)	17.7 (2.4)	6.8 (3.6)
R-merge, ^a %	4.4 (29.5)	4.5 (37.8)	7.5 (20.6)
R-pim, ^b %	2.3 (21.4)	2.1 (24.6)	5.7 (15.2)
CC1/2, %	99.9 (88.6)	99.9 (87.0)	99.1 (96.2)
Molecules per ASU	1	2	4
Refinement			
R _{work} /R _{free} , ^c %	14.9 (24.5)/16.2 (29.0)	17.2 (28.2)/19.7 (30.0)	25.0 (25.5)/29.9 (31.1)
No. of atoms/average B, Å ²			
Protein	1833	3773	7379
Ligands	50	82	173
Solvent	281	348	521
Nonhydrogen atoms	2164	4203	8017
Protein residues	229	473	927
Ramachandran plot, %			
Favored	99.1	99.1	98.2
Outliers	0.00	0.00	0.00
Standard geometry (RMSZ)			
Bond lengths	0.54	0.61	0.25
Bond angles	0.75	0.80	0.47
PDB accession code	7PCA	7PCZ	7PDO

Statistics for the high-resolution shell are shown in parentheses.

^aR_{merge} = $\sum_{hkl} \sum_i |I_i(hkl) - [I(hkl)]| / \sum_{hkl} \sum_i I_i(hkl)$, where $I_i(hkl)$ is the *i*th measurement of reflection *hkl* and $[I(hkl)]$ is the weighted mean of all measurements.

^bR_{pim} = $\sum_{hkl} [1/(N-1)] 1/2 \sum_i |I_i(hkl) - [I(hkl)]| / \sum_{hkl} \sum_i I_i(hkl)$, where *N* is the redundancy for the *hkl* reflection.

^cR_{work}/R_{free} = $\sum_{hkl} |F_o - F_c| / \sum_{hkl} |F_o|$, where F_c is the calculated and F_o is the observed structure-factor amplitude of reflection *hkl* for the working/free (5%) set, respectively.

ASU, asymmetric unit; PDB, Protein Data Bank; RMSZ, root mean square of all zscores of the bond lengths (or angles).

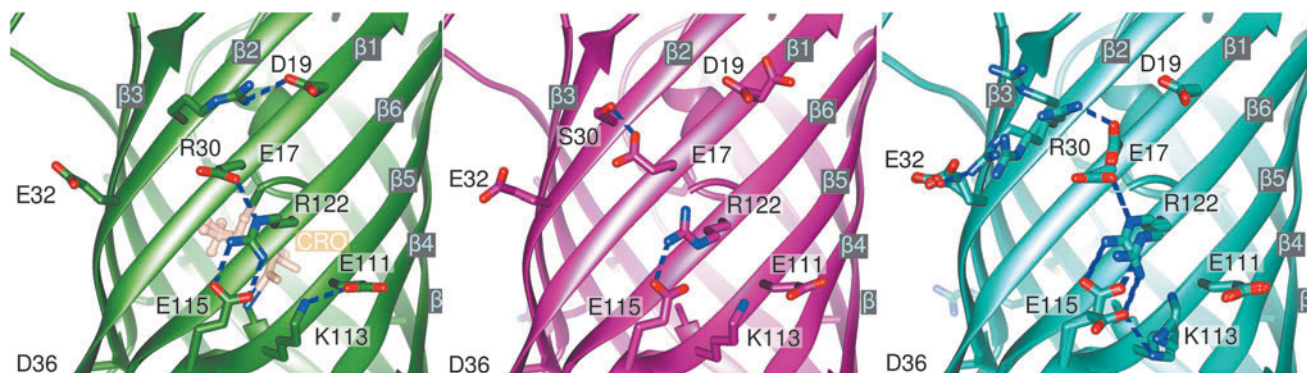


FIG. 2. Close-up of *sfroGFP2*^{WT} (green), *sfroGFP2*^{R30S} (magenta), and *sfroGFP2*^{N39Y} (turquoise). Close-up of the individual barrel centers. Differences in the surroundings of residue R30 (*sfroGFP2*^{WT} and *sfroGFP2*^{N39Y}) or S30 (*sfroGFP2*^{R30S}) result in changes in the network of ionic interactions.

TABLE 2. ENERGIES OF MAJOR PHASE TRANSITIONS OF THE INVESTIGATED VARIANTS

	$sfrGFP2^{WT}$	$GFP_{sfrGFP2}$	$roGFP2_{sfrGFP2}$	$R30S_{sfrGFP2}$	$N39Y_{sfrGFP2}$	$R223F_{sfrGFP2}$
$E_{cut}^{a,b}$	-4.01	-3.88	-4.04	-3.89	-4.07	-3.98
$SEM^{b,c}$	0.07	0.08	0.02	0.03	0.08	0.05

^aValues are averaged over all snapshots of $N=5$ replicas with $N=5000$ snapshots each.

^bIn kcal mol⁻¹.

^cStandard error of the mean across five replicas.

X-ray crystal structure of $sfrGFP2^{WT}$ as a template to perform rigidity analysis. We inserted the relevant substitutions to create structural models of GFP ($GFP_{sfrGFP2}$) and roGFP2 ($roGFP2_{sfrGFP2}$) to explore differences in stability between these variants. Furthermore, the structural models $R30S_{sfrGFP2}$, $N39Y_{sfrGFP2}$, and $R223F_{sfrGFP2}$ were generated based on the $sfrGFP2^{WT}$ template to investigate residue-specific effects.

We hypothesized that the higher FI of $sfrGFP2^{WT}$ in an *in cellulo* environment is associated with the higher structural stability of $sfrGFP2^{WT}$ compared with GFP. To test this hypothesis, we analyzed the different structures with respect to their mechanical stability. We applied principles from rigidity theory. Details about these computations are provided in the Supplementary Methods section.

The computations predict that the major phase transition of $sfrGFP2^{WT}$ ($E_{cut} = -4.01$ kcal mol⁻¹) occurs at an energy E_{cut} 0.13 kcal mol⁻¹ lower than that of $GFP_{sfrGFP2}$ ($E_{cut} = -3.88$ kcal mol⁻¹) (Supplementary Fig. S1 and Table 2; $p=0.13$; two-sided *t*-test, $n=5$), with both variants showing one major phase transition (Supplementary Fig. S2A, C). The result clearly indicates a higher structural stability of $sfrGFP2^{WT}$ than GFP.

To obtain insights at the local, residue-wise level, the averaged constraint dilution trajectory of $GFP_{sfrGFP2}$ (Fig. 3A) was visually inspected, revealing that—except for residue 30—all residues that are exchanged *via* sf mutations in $sfrGFP2^{WT}$ segregate from the giant rigid cluster right before the major phase transition (Fig. 4A). Hence, these residues are structural weak spots that, when appropriately substituted, should increase the structural stability by shifting the phase transition to lower E_{cut} values. Indeed, in $sfrGFP2^{WT}$, the substituted residues segregate at a later point in the constraint dilution trajectory (Fig. 3B).

The sf mutation S30R in $sfrGFP2^{WT}$, which forms a hydrogen bond with D19 in the neighboring β -strand, segregates from the largest rigid cluster during the major phase transition (Fig. 4B). Hence, this interaction is particularly important for the structural integrity of $sfrGFP2^{WT}$. The importance of R30 in $sfrGFP2^{WT}$ is corroborated, in that the phase transition of $R30S_{sfrGFP2}$ is at an E_{cut} value 0.11 kcal mol⁻¹ higher than that of $sfrGFP2^{WT}$ (Supplementary Fig. S1 and Table 2, $p=0.10$) and on a par with that of GFP (Supplementary Fig. S1 and Table 2). Accordingly, reversing this substitution abolishes most of the gain in the structural stability of $sfrGFP2^{WT}$ over GFP. The particular effect of residue 30 is dependent on the residue composition of $sfrGFP2^{WT}$, however (Fig. 4B). $roGFP2_{sfrGFP2}$, which contains S30 from GFP and none of the other sf mutations, is yet similarly resistant to oxidation-like $sfrGFP2^{WT}$, the major phase transition occurs at almost the same E_{cut} as in $sfrGFP2^{WT}$ (Supplementary Fig. S1 and Table 2).

Apparently, the roGFP2 mutations have a different long-range effect based on the changing interactions of the residues in the presence or absence of the sf mutations. In turn, the interactions formed by the sf mutations in $sfrGFP2^{WT}$ alter the constraint network due to interaction partners changing conformation to accommodate the mutations (Fig. 4B). By contrast, $N39Y_{sfrGFP2}$ and $R223F_{sfrGFP2}$ behave similarly to $sfrGFP2^{WT}$ (Supplementary Fig. S1 and Table 2).

The rigidity percolation behavior of protein networks is usually complex, and multiple phase transitions can be

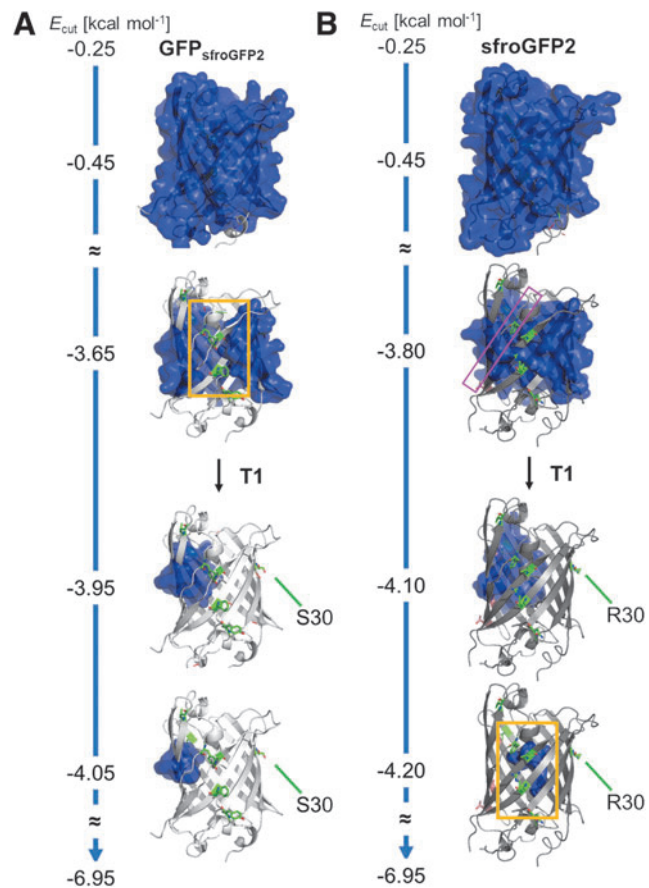


FIG. 3. Constraint dilution trajectory of $GFP_{sfrGFP2}$ (A) and $sfrGFP2^{WT}$ (B) showing one major phase transition. The blue-colored body shows the largest rigid cluster over various energies with the major phase transition T1 indicated with a black arrow. $GFP_{sfrGFP2}$ (light gray) and $sfrGFP2^{WT}$ (dark gray) are shown as cartoons with residues affected by the roGFP2 (salmon) and sf (green) mutations shown as sticks. The pink rectangle indicates the β -strand (residues 142–151) that first loses structural stability. Close-ups of $GFP_{sfrGFP2}$ (Fig. 4A) and $sfrGFP2^{WT}$ (Fig. 4C) are indicated with orange rectangles.

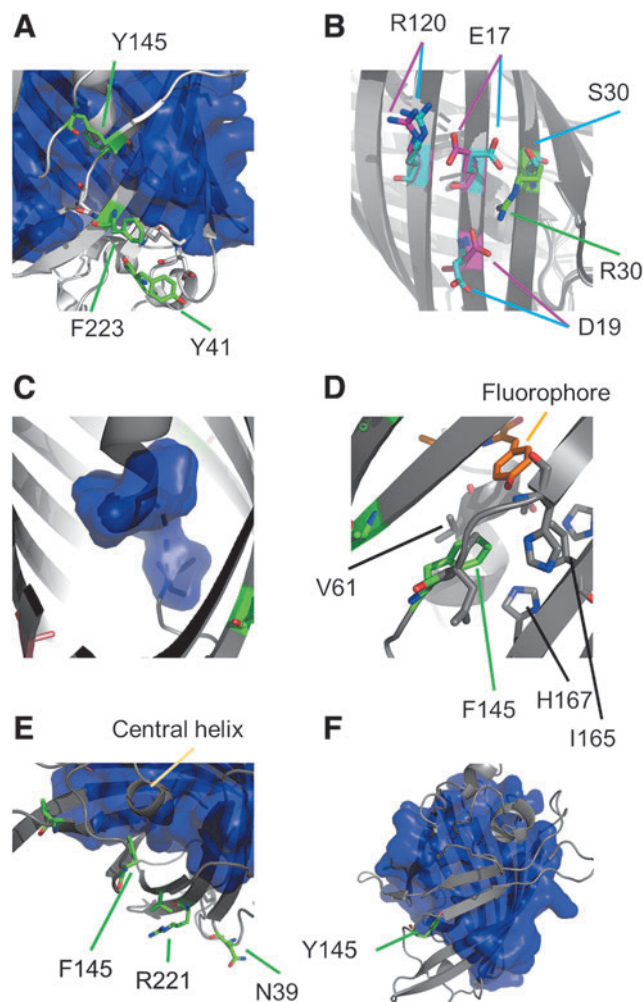


FIG. 4. Close-ups of GFP_{sfroGFP2} and sfroGFP2^{WT} during constraint dilution simulations. The blue-colored body shows the largest rigid cluster in GFP_{sfroGFP2} (light gray cartoon, **A**), sfroGFP2^{WT} (dark gray cartoon, **B–E**), and roGFP2 (medium gray, **B, F**), with the residues affected by the roGFP2 (salmon) and sf (green) mutations shown as sticks. In (**A**), the state of GFP_{sfroGFP2} right before the transition point is shown. In (**B**), roGFP2_{sfroGFP2} and sfroGFP2^{WT} are superimposed. The presence of the sf mutations (green, S30 in roGFP2, R30 in sfroGFP2^{WT}) leads to a different network of the surrounding residues in sfroGFP2^{WT} (magenta) than in roGFP2 (light blue). In (**C**), the fluorophore is the last rigid structure in sfroGFP2^{WT}. In (**D**), the sf mutation Y145F resides in a hydrophobic environment close to the fluorophore. In (**E**), as a result, the β -strand containing Y145F percolates from the largest rigid cluster in sfroGFP2^{WT}. In (**F**), a similar behavior of roGFP2 can be seen in which the β -strand containing Y145 percolates from the largest rigid cluster in roGFP2, while most of the β -barrel, including the chromophore and the central helix, remain rigid.

observed (44, 55). In line with this, besides a shift of the major phase transition point, substitutions in sfroGFP2^{WT} impact later transitions in the constraint dilution trajectory. In GFP_{sfroGFP2}, the last rigid part of the protein is part of the β -barrel and comprises residues T95–F97, F163, K164, and D178–Y180 (Fig. 3A); by contrast, in sfroGFP2^{WT}, the last rigid part of the protein is the fluorophore (Fig. 4C).

These analyses of structural stability reveal a later rigid-to-flexible phase transition during constraint dilution simulations in sfroGFP2^{WT} than in GFP, pinpoint the particular role of the S30R substitution, and suggest that sf mutations increase not only the structural stability of the β -barrel but also of the fluorophore region. To examine the effects of the sf mutations on the biosensors' properties, we performed functional characterization.

Functional properties

Spectral excitation scans were recorded using recombinant sfroGFP2^{WT}, the three reverse mutants sfroGFP2^{R30S}, sfroGFP2^{N39Y}, and sfroGFP2^{R223F}, as well as roGFP2, which served as a reference (Fig. 5A). Fluorescence spectra of roGFP2 (Fig. 5A) were consistent with previously published spectral scans (18, 65). As shown in Figure 5A, the different sf mutations did not affect the dual excitation behavior. For oxidized protein, excitation peaks at 405 and 485 nm are seen. However, the excitation peak at 485 nm is stronger for reduced protein. Therefore, the commonly used excitation maxima for roGFP-based redox measurements can be used identically for sfroGFP2^{WT}- and sfroGFP2-based redox biosensors. Furthermore, the emission scans for all investigated biosensors showed the same emission pattern with maxima at 510 nm (data not shown). These results confirm that the sf mutations do not affect the excitation and emission pattern of the sensors.

In vitro spectral excitation scans using standard potassium phosphate buffer show slightly more intense FI for roGFP2 (FI_{ox405} = 25,000 RFU; FI_{red485} = 100,000 RFU) than for sfroGFP2^{WT} (FI_{ox405} = 16,000 RFU; FI_{red485} = 87,000 RFU) (Fig. 4A, light red and light blue spectra). Moreover, the FI of emission at 510 nm after excitation at 405 and 485 nm was slightly stronger for roGFP2 than for sfroGFP2^{WT} (roGFP2: FI_{510ox} = 17,000 RFU, FI_{510red} = 22,000 RFU; sfroGFP2^{WT} FI_{510ox} = 11,000 RFU, FI_{510red} = 19,000 RFU).

Spectral excitation and emission scans of the reverse mutants sfroGFP2^{R30S}, sfroGFP2^{N39Y}, and sfroGFP2^{R223F} showed the same overall pattern as sfroGFP2^{WT}. All sfroGFP2 variants showed higher FI than sfroGFP2^{WT} *in vitro* for both excitation wavelengths, as well as for emission at 510 nm after excitation at 405 nm and 485 nm. In addition, sfroGFP2^{R30S} and sfroGFP2^{R223F} showed higher FI than roGFP2 (Fig. 5A).

Furthermore, spectral scans were recorded at physiological temperature (37°C) to mimic the conditions for *in cellulo* measurements in *P. falciparum*, where structural stability may be particularly relevant to withstand increased thermal challenge (Fig. 5A, dark red and dark blue spectra). With higher temperatures, the FI of roGFP2 and sfroGFP2^{WT} decreased. However, the reduction in FI was not as pronounced for sfroGFP2^{WT} as for roGFP2. Changes in FI of sfroGFP2^{R30S}, sfroGFP2^{N39Y}, and sfroGFP2^{R223F} were in a comparable range. The sharpest decline in FI_{405ox} was seen for sfroGFP2^{R223F}. The strongest decrease in FI_{485red} was seen for sfroGFP2^{R30S}.

Following the rationale of proximity-based redox sensor specificity introduced by Gutscher *et al.*, sfroGFP2^{WT} was fused to hGrx1 to generate a proximity-based sensor that allows specific and fast equilibration between sfroGFP2^{WT} and the glutathione redox couple (17). The fusion sensor

hGrx1-sfroGFP2 was characterized in comparison with hGrx1-roGFP2. Spectral excitation and emission scans with recombinant biosensors were recorded at 10°C (Fig. 5B, light red and light blue spectra). Here, hGrx1-roGFP2 showed higher FI than hGrx1-sfroGFP2. In addition, spectral scans were performed at physiological temperature (37°C) (Fig. 5B, dark red and dark blue spectra). Here, the FI of hGrx1-roGFP2 decreased, whereas it increased for hGrx1-sfroGFP2. In general, FI were higher for both hGrx1-fusion sensors; that is, roGFP2 and sfroGFP2^{WT}.

To study the spectral response of the sensor variants to oxidation and reduction, as well as the reversibility of the reaction, ratio changes with recombinant roGFP2, hGrx1-roGFP2, sfroGFP2^{WT}, and hGrx1-sfroGFP2 were measured. As shown in Supplementary Figure S3, all biosensors responded rapidly to oxidation with diamide (DIA). The ratio of the fully oxidized biosensors was stable but could be fully reversed *via* reduction with dithiothreitol. No difference in the responsiveness to oxidizing and reducing agents was identified between the individual biosensor variants tested.

We examined the pH responsiveness for all redox biosensors. These responses were monitored over a pH range from 5.0 to 9.0 to cover physiologically meaningful conditions. The ratios of all biosensors were unaffected by pH across the range from 6.0 to 8.0; only a minor impact started to become apparent at acidic pH values <6.0 (Fig. 6). These data confirm that pH insensitivity, as a major advantage of roGFP-based redox sensors, is retained in the sensor variants.

Redox titrations were performed for all redox biosensors, using the dithiothreitol (DTT)/dithian system, to determine the midpoint potentials (Fig. 7). Midpoint potentials for roGFP2 have been empirically determined and vary somewhat depending on the specific protocol used (−272 mV vs. −284 mV). Therefore, a consensus midpoint potential of roGFP2 was defined at −280 mV (12, 18, 39). Our results are in accordance with this as the midpoint potential of roGFP2 within our measurements was -280.3 ± 0.4 mV. Moreover, we found that the different sf mutations did not change the midpoint potential of the sensor to any major extent as the midpoint potential of sfroGFP2^{WT} is -283.6 ± 0.5 mV. The midpoint potentials of hGrx1 fusion and the other sensor variants are also largely retained, and are only slightly more negative; with -287.1 ± 0.4 mV for hGrx1-roGFP2, -285.8 ± 0.4 mV for hGrx1-sfroGFP2, -283.9 ± 0.2 mV for sfroGFP2^{R30S}, -286.8 ± 0.7 mV for sfroGFP2^{N39Y}, and -284.8 ± 0.4 mV for sfroGFP2^{R223F}.

In cellulo use of redox biosensors

SfroGFP2^{WT} was stably integrated into the genome of NF54attB *Plasmodium falciparum* clone (*P. falciparum*) through integrase-mediated homologous recombination

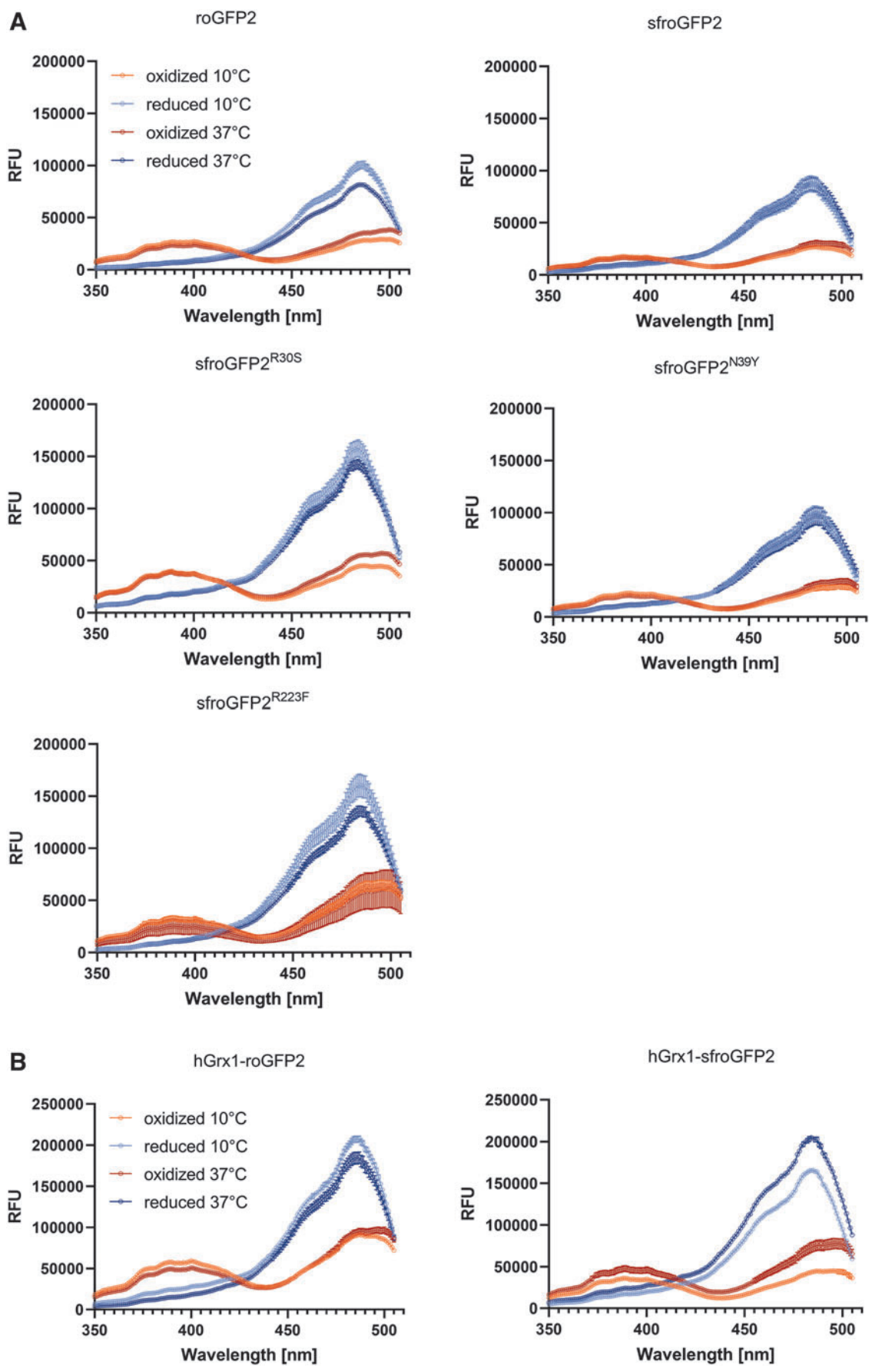
between the parasite's attB site and the plasmid's attP site (43) as previously described by Schuh *et al.* (64). Spectral excitation scans of NF54attB^{sfroGFP2} showed normal roGFP2 behavior with strong FI and an improved signal-to-noise ratio (Supplementary Fig. S4). These results are in agreement with earlier published data (64). Furthermore, we stably integrated the fusion sensor hGrx1-sfroGFP2 into the genome of NF54attB *P. falciparum* parasites because it was shown that the equilibration between sfroGFP2 with the glutathione couple is faster in different cellular contexts, and the kinetics is standardized when the sensor is fused to glutaredoxin (17, 64).

For comparison, we used an NF54attB parasite line stably expressing hGrx1-roGFP2 (64). Lines are referred to as NF54attB^{hGrx1-sfroGFP2} and NF54attB^{hGrx1-roGFP2} throughout the article. All parasite lines used in this study expressed the sensors cytosolic. As shown in Figure 8, FI for NF54attB^{hGrx1-sfroGFP2} was strongly increased when compared with NF54attB^{hGrx1-roGFP2}. WT NF54attB parasites were used to adjust the FI by subtracting the background fluorescence of the parasites and the surrounding red blood cell. A difference in FI between *in vitro* and *in cellulo* measurements is clearly visible here. While the spectral properties of the recombinant sfroGFP2^{WT} do not seem to be better, the measurements with parasites show a clearly improved FI. These data show an improved signal-to-noise ratio and an enhanced FI of sfroGFP2-based biosensors over roGFP2-based biosensors *in cellulo*.

Since the FI of both hGrx1-sfroGFP2 and sfroGFP2^{WT} was ~3x higher than that of hGrx1-roGFP2 *in cellulo* (Fig. 7 and Supplementary Fig. S4), while both sensor proteins showed similar FI *in vitro* (Fig. 5), we hypothesized that more mature and functional sf sensor protein was present due to enhanced expression, proportion of maturation, or stability. To test this hypothesis, Western blot analysis was performed to examine the expression levels of the different sensors. NF54attB^{hGrx1-roGFP2}, NF54attB^{sfroGFP2}, and NF54attB^{hGrx1-sfroGFP2} parasites were examined.

All investigated proteins of interest were detected in full length. All samples showed a GFP signal with the expected size (Supplementary Fig. S5). Band intensity between the samples NF54attB^{hGrx1-roGFP2} and NF54attB^{sfroGFP2} differed by $-2.3\% \pm 11.2\%$. The difference in band intensity between the samples NF54attB^{hGrx1-roGFP2} and NF54attB^{hGrx1-sfroGFP2} was $-28.7\% \pm 20.8\%$. Anti-PfHSP70 antibody (AB) was used as a loading control (Supplementary Fig. S5). This analysis showed that expression levels between the sensors only differed slightly, with NF54attB^{hGrx1-roGFP2} showing the highest expression level. Thus, degree of maturation and/or stability of folding, as indicated by the rigidity analysis of sensor structure, appear to be responsible for the improved *in cellulo* performance rather than protein abundance.

FIG. 5. Spectral excitation scans of various redox biosensor variants. (A) Spectral excitation scans of sfroGFP2^{WT}, sfroGFP2^{R30S}, sfroGFP2^{N39Y}, and sfroGFP2^{R223F} in comparison with roGFP2. Sensors were fully oxidized using 1 mM DPS (red curves) or fully reduced using 10 mM DTT (blue curves) before measurement. (B) Spectral excitation scans of hGrx1-roGFP2 and hGrx1-sfroGFP2. Sensors were fully oxidized using 1 mM DPS (red curves) or fully reduced using 10 mM DTT (blue curves). Light red and light blue spectra indicate measurements carried out at ~10°C; dark red and dark blue spectra indicate measurements carried out at 37°C. For details, see the Materials and Methods section. DPS, 2,2'-dithiopyridylsulfide; DTT, dithiothreitol; hGrx1, human glutaredoxin-1; RFU, random fluorescence intensity units; roGFP, reduction/oxidation-sensitive green fluorescent protein; sfroGFP2, superfolder reduction/oxidation-sensitive green fluorescent protein.



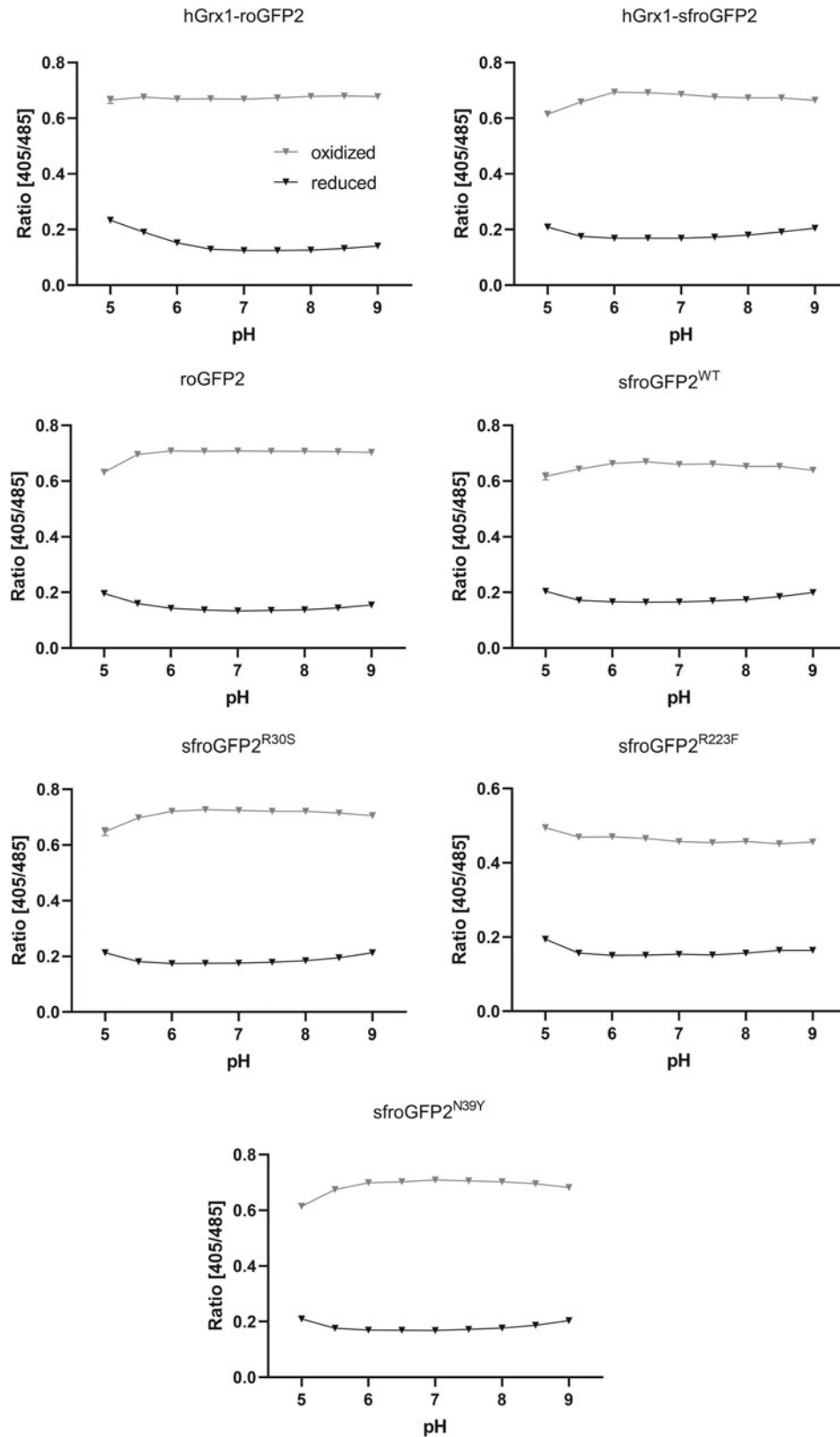


FIG. 6. pH response of different biosensor variants. Recombinant sensor proteins were equilibrated in buffers with pH values varying between 5.0 and 9.0. All biosensor proteins were fully reduced and fully oxidized using 10 mM (DTT [black] and 1 mM DPS [gray], respectively). Means \pm standard error are shown. $N=4$.

Discussion

In this work, we aimed to identify the molecular basis for the improved fluorescence properties of sfroGFP2^{WT} as this knowledge provides important insights for future sensor

developments. To achieve this goal, we characterized different redox biosensor variants *in vitro* and *in cellulo*.

In previous studies in which we described the redox biosensor sfroGFP2^{WT}, we demonstrated an improved FI *in cellulo* (64), which could be confirmed in this study.

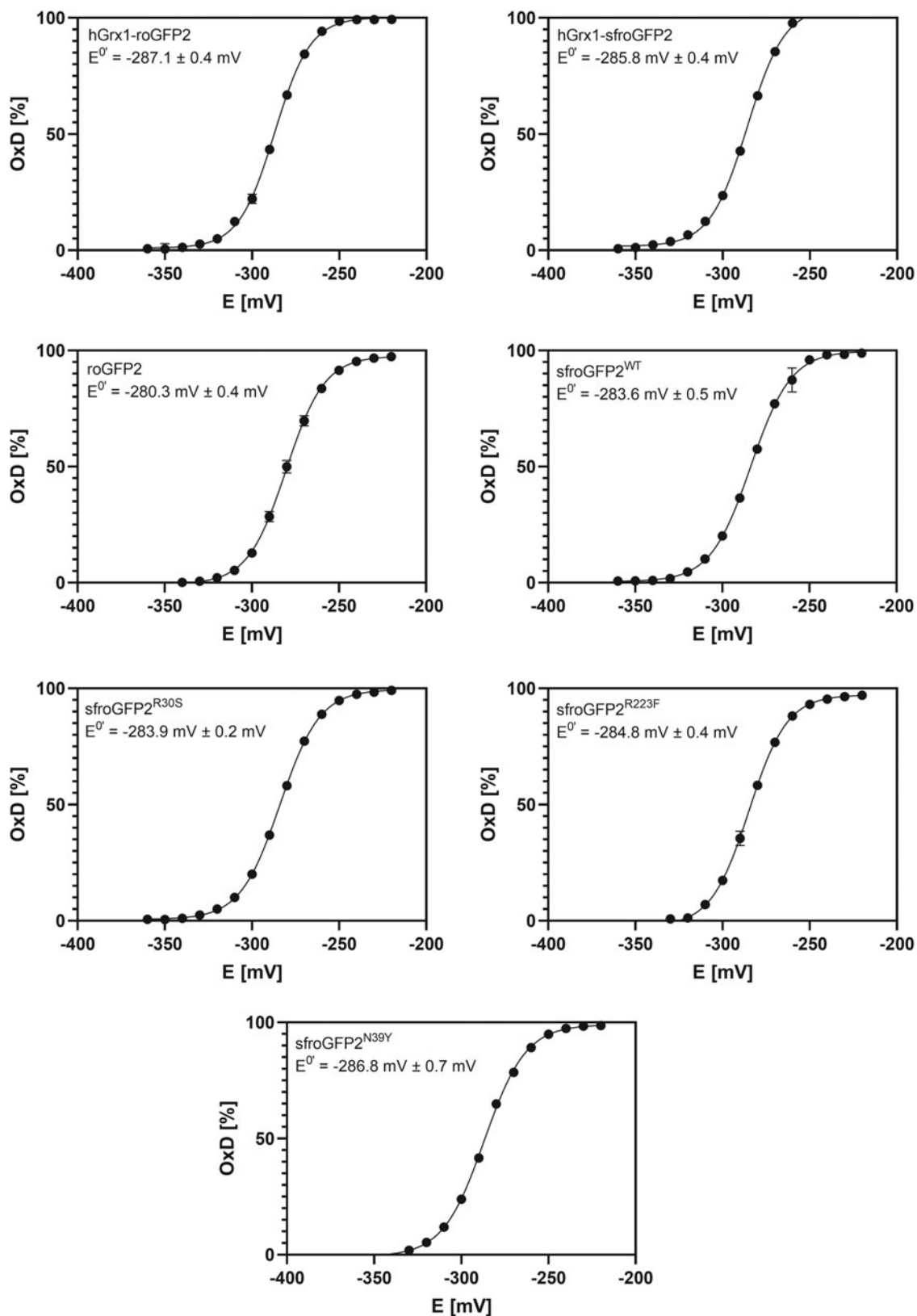


FIG. 7. Redox titration of different biosensor variants. Specific redox potentials were adjusted using different mixtures of dithiothreitol (DTT_{red}) and dithian (DTT_{ox}), calculated from the Nernst equation. Biosensor proteins were allowed to equilibrate in the different buffers, and were also fully reduced (10 mM DTT) and fully oxidized (1 mM DPS). Means with error bars indicating standard deviation are shown. $N=4$.

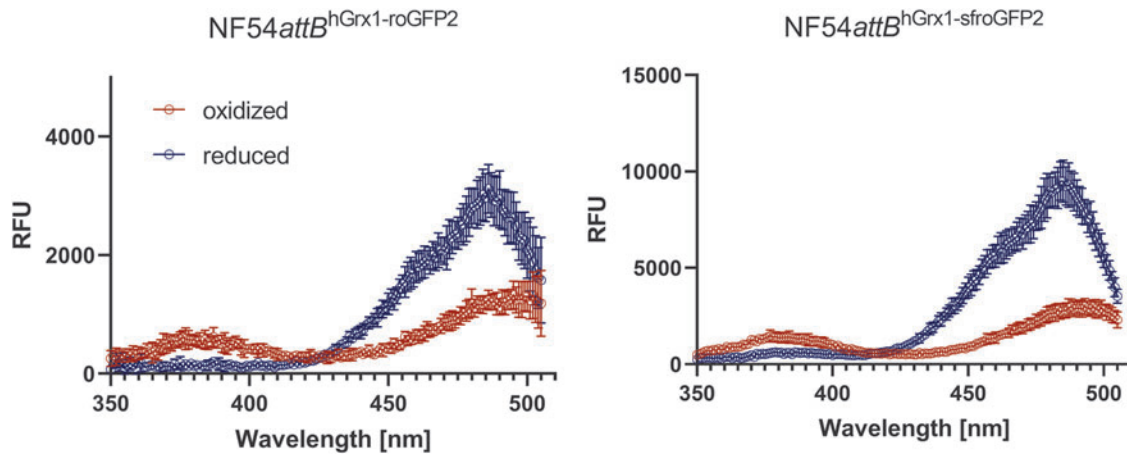


FIG. 8. Spectral excitation scans of $NF54attB^{hGrx1-roGFP2}$ and $NF54attB^{hGrx1-sfroGFP2}$. For spectral excitation scans, the sensor was fully reduced by treating the parasites with 10 mM DTT (blue curve) and fully oxidized via treatment with 1 mM DIA (red curve). 2.0×10^6 parasites each per measurement were used. $N=4 \pm SD$. DIA, diamide.

P. falciparum parasites stably expressing $sfroGFP2^{WT}$ or $hGrx1-sfroGFP2$ showed improved FI compared with parasites expressing $hGrx1-roGFP2$. Enhanced expression levels of $(hGrx1)-sfroGFP2$ could be excluded as a cause of the improved FI via Western blot analysis as the expression levels of all sensor proteins investigated here were comparable. Subsequently, further *in vitro* investigations were carried out.

During the development of $sfroGFP2^{WT}$, we aimed to improve the FI of the redox biosensor, but without affecting other sensor properties. We therefore investigated the pH responsiveness of the different sensor variants and determined their midpoint potential. All redox biosensor variants are pH insensitive at physiologically meaningful pH values between 6.0 and 8.0, and show midpoint potentials similar to $roGFP2$ -based biosensors, making them suitable sensors for measuring oxidizing effects within the cytosol and most of the subcellular compartments of *Plasmodium* parasites. *In cellulo*, the use of $sfroGFP2^{WT}$ fused to $hGrx1$ seems to be wiser, since it allows reactions with GSH and GSSG to proceed much more effectively (64).

Unexpectedly, *in vitro* spectral scans showed a diminished FI for recombinant $(hGrx1)-sfroGFP2^{WT}$ compared with recombinant $(hGrx1)-roGFP2$ using standard conditions. We investigated this effect in more detail and performed spectral scans at different temperatures. We observed a more stable FI for $sfroGFP2$ -based biosensors at higher temperatures ($37^\circ C$), which are required for *in cellulo* measurements with *Plasmodium* parasites. In general, the FI of both $hGrx1$ -fusion sensors were higher. We therefore hypothesize a potentially stabilizing effect of $hGrx1$, improving the FI of the actual sensor. Stabilizing effects of Trx—which features Grx fold—have already been described (36). These advantageous properties are used for protein expression and purification. Here, Trx is used as a fusion protein to prevent protein aggregation and to increase the folding behavior of the protein of interest (36).

Protein–protein interactions occurring within the parasites could be excluded to be the only responsible factor for the differences in *in vitro* and *in cellulo* experiments. This was

studied on the basis of spectral scans using recombinant protein equilibrated in buffer or parasite cell extract (data not shown). Nevertheless, the environment within an intact parasite differs strongly from standard buffer or lysed parasites. The concentration of different molecules as well as their interaction with each other or with membranes cannot be fully remodeled *in vitro*. As discussed by Minton and colleagues, molecular crowding can lead to large differences between *in vitro* and *in vivo* measurements (40, 59). However, not only the surrounding cellular milieu can differ; furthermore, different host cells used for expression can influence protein stability and their properties (11, 42). Therefore, findings from *in vivo* or *in cellulo* measurements cannot always be explained with *in vitro* examinations.

For fluorescent proteins, the structural stability of the fluorophore is especially important to maintain the conjugated π -electron system and the dipole moment, which are important for fluorescence (35). Therefore, we examined differences in structural stability between $roGFP2$ and $sfroGFP2^{WT}$ using X-ray crystal structure analysis and rigidity analysis.

Our results, based on rigidity analysis, demonstrate that both $roGFP2$ and $sfroGFP2^{WT}$ show an improved structural stability over GFP. However, the sf mutations in $sfroGFP2^{WT}$ lead to a different conformation of residues than in $roGFP2$, resulting in disparate interaction networks between the two variants. Pédelacq *et al.* have already suggested that among all sf mutations, S30R and Y39N have the greatest impact on folding stability (45). We have studied the effects of these specific sf mutations on protein stability in more detail by reversing them in the crystal structures of $sfroGFP2^{R30S}$ and $sfroGFP2^{N39Y}$, as well as their models $R30S_{sfroGFP2}$ and $N39Y_{sfroGFP2}$, for rigidity analysis.

We focused our efforts on these specific mutations and their impact on the protein stability. However, one has to mention that for $roGFP$ -biosensors the H-bond involving E222 has also a major impact on the chromophore. Due to the S65T mutation, which is present in all redox biosensors derived from enhanced GFP, the H-bond network that stabilizes the neutral chromophore is disrupted, leading to a shift

in equilibrium toward the anionic form. In roClover, a redox biosensor variant that includes the sf mutations as well, the conformation of E222 differs slightly. However this is not because of the sf mutations. Moreover, both the mutations T65G and T203H present in roClover—but not roGFP2 or sfroGFP2^{WT}—are rather responsible therefore. However, these specific mutations have the same effect as S65T that is present in both roGFP2 and sfroGFP2^{WT} (4).

We therefore focused on the sf mutations S30R and Y39N. Our crystal structures of sfroGFP2^{WT} show that the barrel and the chromophore are at most marginally shifted in their position, but an ion network between the strands is formed by inclusion of the sf mutation S30R, which probably increases the stability of sfroGFP2^{WT}. Even though both sf mutations cause an interaction between AA of adjacent strands, probably improving the stability of the barrel, we assume that the influence of the substitution at position 30 is much more critical than that at position 39 due to the more complex network in the surrounding of residue 30.

Our sfroGFP2^{R30S} and sfroGFP2^{N39Y} structures confirm these findings; in particular, reversing the sf mutation S30R in the crystal structure of sfroGFP2^{R30S} disrupts the ion pair network between adjacent strands. Even though we only saw slight structural differences between our crystal structures of sfroGFP2^{WT} and sfroGFP2^{R30S}, by using rigidity analysis, we were able to confirm that the sf mutation S30R is important for the stability of sfroGFP2^{WT}. Reversing the sf mutation S30R in the structural model R30S_{sfroGFP2} has a major impact on the overall stability of the protein, reducing the stability close to the level of GFP.

Besides stabilizing the β -barrel structure, the sf mutations in sfroGFP2^{WT} exert a long-range effect on the barrel center, such that the fluorophore remains structurally stable until the end of the constraint dilution simulations, whereas in GFP the fluorophore becomes unstable.

Taken together, our data confirm the hypothesis that variants with a higher resilience against oxidative alterations have a more stable structure under the experimental conditions chosen. The constraint dilution simulations explain this higher structural stability of roGFP2 and sfroGFP2^{WT} over GFP on a per residue level, including the fluorophore in sfroGFP2^{WT}, and thus can rationalize the higher stability and FI of these variants in changing redox conditions. These findings were in line with other studies showing a higher resilience of more structurally stable proteins (16, 23, 38, 44, 46), although this relation is not undebated (31).

The knowledge generated in this study about the molecular basis underlying the improved FI of sfroGFP2^{WT}-based redox biosensors *in cellulo* compared with roGFP2-based biosensors can be applied to other sensors, and can thus enrich the field of sensor development.

Materials and Methods

Drugs and chemicals

All chemicals used were of the highest available purity and were obtained from Thermo Fisher Scientific (Dreieich, Germany), Roth (Karlsruhe, Germany), Sigma-Aldrich (Steinheim, Germany), or Merck (Darmstadt, Germany). RPMI 1640 medium was purchased from Gibco (Paisley, United Kingdom) and SYBR Green I from Thermo Fisher Scientific.

Engineering sfroGFP2 mutants

To generate sfroGFP2^{R30S}, sfroGFP2^{N39Y}, and sfroGFP2^{R223F}, site-directed mutagenesis PCR was performed using pQE30-[sfroGFP2^{WT}] as a template, AccuPrime™ Pfx DNA polymerase (Thermo Fisher Scientific, Waltham, MA), and specific primer pairs (Supplementary Table S1). Template plasmids were digested using *DpnI* (Thermo Fisher Scientific). Correctness of mutants was verified by sequencing (LGC genomics).

Expression and purification of recombinant redox biosensors

The different redox biosensors were heterologously overexpressed using *Escherichia coli* (*E. coli*) cells. RoGFP2 was expressed in lysogeny broth (LB) medium using *E. coli* M15 [pREP4] cells (kanamycin resistance, Kan^R), which were transformed with roGFP2 in pQE30 (carbenicillin resistance, Cn^R), at 37°C for 4 h. HGrx1-roGFP2 was produced as described by Kasozi *et al.* (32). SfroGFP2^{WT} and hGrx1-sfroGFP2 were produced according to Schuh *et al.* (64). For heterologous overexpression of the sfroGFP2 mutants, *E. coli* M15 [pREP4] cells (Kan^R) were transformed with either pQE30-[sfroGFP2^{R30S}], pQE30-[sfroGFP2^{R223F}], or pQE30-[sfroGFP2^{N39Y}] (Cn^R, respectively).

SfroGFP2^{R30S} and sfroGFP2^{R223F} were expressed in LB medium at 37°C or room temperature (RT) for 4 h. SfroGFP2^{N39Y} was expressed in terrific broth medium at 37°C for 2 h. Pellets were harvested *via* centrifugation and stored at -20°C. Frozen pellets were thawed, resuspended in HEPES buffer (50 mM HEPES, 300 mM NaCl, pH 7.5), and mixed with protease inhibitors (150 nM pepstatin, 40 nM cystatin, 100 μ M phenylmethylsulfonyl fluoride). After lysis using lysozyme, DNase, and sonication, supernatants were obtained *via* centrifugation (18,000 rpm, 30 min, 4°C). After purification of all proteins *via* hexahistidyl affinity chromatography on Ni-NTA and fast protein liquid chromatography, they were concentrated using 10 or 30 kDa Vivaspins columns (Sartorius, Göttingen, Germany) and stored at 4°C.

Crystallization, data collection, and processing of recombinant redox biosensors

SfroGFP2^{WT}, sfroGFP2^{R30S}, and sfroGFP2^{N39Y} crystals were grown in white light at 22°C in sitting drops with the vapor diffusion technique, using a Honeybee 961 crystallization robot. For crystallization of sfroGFP2^{WT}, the protein was concentrated in 300 mM NaCl and 0.05 M Hepes (pH 7.5) to 30 mg/mL. In the drop, 0.2 μ L of protein solution was mixed with 0.2 μ L reservoir solution (46% v/v EtOH, 0.25% v/v dichloromethane). Crystals appeared after 1 day at RT. Before data collection, crystals were soaked in mother liquor with a final concentration of 15% glycerol. Diffraction data for all crystals were collected at X10SA (detector: Pilatus) from the Swiss Light Source in Villigen, Switzerland.

Diffraction data were collected at 100K and processed with XDS (30). The orthorhombic crystals diffracted up to 1.1 Å resolution and obeyed P2₁2₁2₁ space group symmetry with one monomer in the asymmetric unit. SfroGFP2^{R30S} was crystallized using 0.2 μ L of 30 mg/mL protein and 0.2 μ L of 10% polyethylene glycol (PEG) 6000, 30% ethanol and

100 mM sodium acetate. After 1 day, crystals appeared at RT. The X-ray structure was solved with a resolution of 1.35 Å. For sfroGFP2^{N39Y}, 0.2 μL of 30 mg/mL protein was mixed with 0.2 μL 30% PEG 4000. Crystals appeared after 5 days. The structure was solved with a resolution of 2.0 Å.

Structure determination

The structure was solved *via* molecular replacement. The search model was generated *via* homology modeling with SWISS-MODEL (72). As a template for modeling, we used the structure of *A. victoria* GFP (Protein Data Bank code 1qyo), which shares a sequence identity of 94% with sfroGFP2^{WT}. The first refinement of the molecular replacement solution revealed an R_{free} of 25%. During refinement, 6% of all reflections were omitted and used for calculating an R_{free} value. We improved the models in cycles of manual building and refinement, with a final R_{free} of 16.2%. Data collection and refinement statistics are shown in Table 1. The PHENIX program suite (1) was used for reflection phasing and structure refinement. The interactive graphics program Coot (14) was used for model building. Molecular graphics images were produced using the UCSF Chimera package (47).

Rigidity analysis

Generation of structural models. The X-ray crystal structure of sfroGFP2^{WT} was used to generate structural models of R30S_{sfroGFP2}, N39Y_{sfroGFP2}, R223F_{sfroGFP2}, roGFP2_{sfroGFP2}, and GFP_{sfroGFP2}. The respective structural models were generated based on one template structure and with the same structural modeling technique to minimize these influences on the outcome of subsequent computations (49, 58). This modeling was performed with Maestro as described below.

Molecular dynamics simulations. In all cases, Maestro (Schrödinger, LLC, New York, 2017) was used for introducing substitutions, and protonation states were assigned with PROPKA (2) at pH 7.4. Using tleap from the Amber18 package of molecular simulation software (5), the systems were neutralized by adding counter ions and solvated in an octahedral box of TIP3P water (27) with a minimal water shell of 12 Å around the protein.

Molecular dynamics (MD) simulations were performed with Amber18 (5). The ff14SB force field (37) was used to parameterize the protein, Joung and Chetham parameters (29) were used for the counter ions, and TIP3P (27) for the water. The fluorophore was parameterized using antechamber (71), prepregen, and parmchk2, which are part of Amber18, following the procedure described here: <http://ambermd.org/tutorials/basic/tutorial5/index.htm> (see Supplementary Information for topology and force field information). To cope with long-range interactions, the Particle Mesh Ewald method (10) was used; the SHAKE algorithm (62) was applied to bonds involving hydrogen atoms. As hydrogen mass repartitioning (22) was utilized, the time step for all MD simulations was 4 fs with a direct-space, nonbonded cutoff of 8 Å.

At the beginning, 17,500 steps of steepest descent and conjugate gradient minimization were performed; during 2500, 10,000, and 5000 steps, positional harmonic restraints with force constants of 25 kcal/(mol·Å²), 5 kcal/(mol·Å²), and 0, respectively, were applied to the solute atoms. Thereafter, 50 ps of NVT (constant number of particles,

volume, and temperature) MD simulations were conducted to heat up the system to 100 K, followed by 300 ps of NPT (constant number of particles, pressure, and temperature) MD simulations to adjust the density of the simulation box to a pressure of 1 atm and to heat the system to 300 K.

During these steps, a harmonic potential with a force constant of 10 kcal/(mol·Å²) was applied to the solute atoms. As the final step in thermalization, 300 ps of NVT-MD simulations were performed, while gradually reducing the restraint forces on the solute atoms to zero within the first 100 ps of this step. Afterward, five independent production runs of NVT-MD simulations with 2 μs length each were performed. For this, the starting temperatures of the MD simulations at the beginning of the thermalization were varied by a fraction of a Kelvin.

Structures were extracted from the trajectories every 2 ns using cpptraj (60, 61).

Constrained network analysis

The extracted structures were postprocessed using Constraint Network Analysis (CNA) (48) as described in Nutschel *et al.* (44). In short, for analyzing the rigid cluster decomposition of all GFP variants, a constraint dilution simulation was performed using CNA on an ensemble of network topologies generated from an MD trajectory (ENT^{MD}). The ensemble-based CNA was pursued to increase the robustness of the rigidity analyses (48, 58). Subsequently, the unfolding trajectory was visually inspected using VisualCNA (57) for identifying secondary structure elements that segregate from the largest rigid cluster at each major phase transition. VisualCNA is an easy-to-use PyMOL plugin that allows setting up CNA runs and analyzing CNA results, linking data plots with molecular graphic representations (57). See Supplementary Information for more details.

Functional properties

Fluorescence spectra. Spectral scans were performed using a plate reader (CLARIOstar; BMG Labtech, Ortenberg, Germany). Redox biosensor variants were diluted to 1 μM protein concentration in potassium phosphate buffer (100 mM potassium phosphate, 100 mM NaCl, 0.5 mM Na₂-EDTA, pH 7.0). Sensor surface Cys were driven to full reduction using 10 mM DTT or to full oxidation using 1 mM 2,2-dithiopyridylsulfide (DPS). Excitation scans were recorded at 530 ± 10 nm emission, and emission scans after excitation at 405 ± 10 and 485 ± 10 nm, respectively. For measurements at 10°C, precooled buffer, recombinant proteins, and DTT/DPS stock solutions were used. For measurements at 37°C, the buffer and plate reader were preheated. Four technical replicates were performed.

Dynamic change of ratio. The different redox biosensor proteins (roGFP2, hGrx1-roGFP2, sfroGFP2^{WT}, and hGrx1-sfroGFP2) were prerduced using 10 mM DTT and desalted using Bio-Gel P-6 gel (Bio-Rad, Feldkirchen, Germany) resuspended in potassium phosphate buffer (100 mM potassium phosphate, 100 mM NaCl, 0.5 mM Na₂-EDTA, pH 7.0). Redox biosensors were diluted to a final concentration of 1 μM protein in potassium phosphate buffer. Buffer and plate reader were preheated to 37°C. Redox biosensors were excited sequentially at 400 ± 10 and 482 ± 16 nm with

emission at 530 ± 40 nm in a plate reader (CLARIOstar; BMG Labtech). FI were measured every 20 s for 240 s. After 80 s at baseline measurement with prereduced sensor protein, 1 mM DIA was added, and oxidation was monitored for 80 s before reduction by adding 10 mM DTT. Ratios were plotted against time using GraphPadPrism8. Three independent repetitions were performed using sensor protein from three different batches.

pH response. The different redox biosensors were equilibrated in buffers adjusted to pH values ranging from 5.0 to 9.0 (pH 5.0 to pH 6.5, 10 mM MES-KOH, 100 mM NaCl, 5 mM EDTA; pH 7.0 to pH 8.0, 100 mM Hepes-KOH, 100 mM NaCl, 5 mM EDTA; pH 8.5 to pH 9.5, 100 mM Tris-HCL, 100 mM NaCl, 5 mM EDTA). Redox biosensor variants were excited sequentially at 400 ± 5 and 482 ± 8 nm in a plate reader (CLARIOstar; BMG Labtech). All pH points were measured for oxidized (1 mM DPS) and reduced (10 mM DTT) sensor proteins using four technical replicates each.

Redox titration. To determine the midpoint potentials, redox sensors were equilibrated (1 h) with DTT buffers (reduced form 1,4-dithiothreitol, DTT_{red} ; oxidized form 1,3-dithiane, DTT_{ox}). DTT_{red}/DTT_{ox} was used in a total concentration of 10 mM in degassed HEPES buffer (100 mM Hepes, 100 mM NaCl, 0.5 mM Na_2 -EDTA, pH 7.0). The relation of DTT_{red} and DTT_{ox} to set a certain redox potential was calculated with the Nernst equation based on the standard reduction potential of DTT ($E^{0'}_{DTT}$), -330 mV [Eq. (1)]:

$$E^{DTT} = E^{0'}_{DTT} - 2.303 \frac{RT}{zF} \log \frac{DTT_{red}}{DTT_{ox}}. \quad \text{Eq. (1)}$$

R is the gas constant [8.315 J/(K·mol)]; T is the absolute temperature (310.45K); z is the number of transferred electrons (2); F is the Faraday's constant ($96,485^\circ\text{C mol}^{-1}$).

Redox potentials ranging from -220 to -360 mV were adjusted. In addition, redox sensors were fully reduced (10 mM DTT) and fully oxidized (1 mM DPS). Redox sensors were excited sequentially at 400 ± 5 and 482 ± 8 nm in a plate reader (CLARIOstar; BMG Labtech). The degree of oxidation (OxD) was determined according to Equation (2):

$$\text{OxD} = \frac{R - R^{red}}{\frac{I_{485ox}}{I_{485red}} (R^{ox} - R) + (R - R^{red})}. \quad \text{Eq. (2)}$$

R represents the ratio of the FI measured at 405 and 485 nm ($R = \frac{405 \text{ nm}}{485 \text{ nm}}$); R_{red} and R_{ox} are the ratios of the FI of fully reduced or fully oxidized protein; I_{485ox} is the FI at 485 nm for fully oxidized protein; I_{485red} is the FI at 485 nm for fully reduced protein.

To determine the midpoint potential $E^{0'}$ for the different roGFP2 variants, OxD_{roGFP2} was plotted against the calculated redox potential, which was adjusted with DTT_{red}/DTT_{ox} . Using GraphPadPrism8, all data points were fitted to a sigmoidal dose–response curve.

In cellulo characterization of redox biosensor variants

Spectral scan in cellulo. Spectral scans were performed using NF54attB parasites stably expressing hGrx1-roGFP2, sfroGFP2^{WT}, or hGrx1-sfroGFP2. Parasites were cultured (69)

and prior to measurement synchronized with 5% sorbitol. Trophozoite stage parasites were magnetically enriched and diluted in Ringer's solution (122.5 mM NaCl, 5.4 mM KCl, 1.2 mM $CaCl_2$, 0.8 mM $MgCl_2$, 11 mM D-glucose, 25 mM HEPES, 1 mM NaH_2PO_4 , pH 7.4) (100,000 parasites/ μL). Parasites were fully reduced using 10 mM DTT or fully oxidized using 1 mM DIA. Emission and excitation scans were recorded using a plate reader (CLARIOstar; BMG Labtech), with four technical repeats each. Spectra were plotted using GraphPadPrism8.

Western blot analysis. NF54attB^{hGrx1-roGFP2}, NF54attB^{sfroGFP2}, and NF54attB^{hGrx1-sfroGFP2} parasites were synchronized using sorbitol. Trophozoite stage parasites were harvested *via* saponin lysis. After washing three times with phosphate-buffered saline, parasites were lysed using M-PERTM buffer (Thermo Fisher Scientific). Parasite supernatants were mixed with 4× sample buffer with DTT and incubated for 5 min at 95°C. Samples were separated using SDS-PAGE (sodium dodecyl sulfate–polyacrylamide gel electrophoresis) and blotted to a nitrocellulose membrane. After blocking with 5% milk, the membrane was incubated with an anti-GFP AB (1:500 in 5% milk); an antimouse AB conjugated with horseradish peroxidase (HRP) was used as a secondary AB (1:10,000 in 5% milk). After the reaction with luminol, chemiluminescence was detected using an iNTAS ECL Chemostar. Then, the membrane was stripped using the restoreTM PLUS Western blot stripping buffer (Thermo Fisher Scientific).

After blocking with 5% milk overnight, the membrane was incubated with an anti-HSP70 AB (1:500 in 5% milk) as a loading control. Antirabbit AB (1:2000 in 5% milk) conjugated with HRP was used as a secondary AB. Chemiluminescence was detected as described above (Supplementary Fig. S6). Two biological replicates in two technical replicates were performed. Background subtraction using the rolling ball algorithm was performed with Fiji (63). Band intensities were measured using Fiji. GFP signal was normalized by the associated PfHSP70 loading control. Fold change of band intensity and the percentage change of the expression level between NF54attB^{hGrx1-roGFP2} and NF54attB^{sfroGFP2}, as well as NF54attB^{hGrx1-roGFP2} and NF54attB^{hGrx1-sfroGFP2}, were calculated.

Confocal laser scanning microscopy imaging. To record confocal laser scanning microscopy images, parasites were prepared as described by Schuh *et al.* (64). In brief, trophozoite stage parasites were magnetically enriched and washed with prewarmed (37°C) Ringer's solution. Parasites were seeded on poly-L-lysine-coated μ -slides VI (ibidi). Images were taken using a Leica confocal system TCS SP5 inverted microscope equipped with the objective HCX PL APO 63.0×1.30 GLYC 37°C ultraviolet connected to a 37°C temperature chamber.

Samples were excited with a sequential scan at 405 and 488 nm; emission was detected at 500–550 nm. Scanning was performed at 400 Hz frequency and at a 512×512 pixel resolution. The argon laser power was set to 20%; smart gain and smart offset were 950 V and -0.9% , respectively. Images were processed using Fiji. The background was subtracted using the rolling ball algorithm, and contrast was enhanced by 0.01%. To improve the recognizability, colors from the green and red channels were set to yellow and magenta and merged.

Acknowledgments

The authors gratefully acknowledge Michaela Stumpf, Marie Sorg, and Norma Schulz for their technical assistance. Furthermore, they thank Ilme Schlichting and Mirosław Tarnawski for their thoughtfully arranged data collection. Diffraction data were collected at beamline X10SA, Swiss Light Source, Paul Scherrer Institute, Villigen, Switzerland, and they thank the beamline staff for the excellent setup. They are grateful for computational support and infrastructure provided by the *Zentrum für Informations- und Medientechnologie* (ZIM) at the Heinrich Heine University Düsseldorf and the computing time provided by the John von Neumann Institute for Computing (NIC) to HG on the supercomputer JUWELS at Jülich Supercomputing Centre (JSC) (User ID: HKF7, VSK33).

Authors' Contributions

K.F.W., K.B., M.S., H.G., and J.P. directed the overall research program; K.C.H., C.G., A.K.S., and T.N. conducted the experiments; K.F.W., K.C.H., and C.G. analyzed the data and prepared figures; all authors contributed to experimental design, and wrote and edited the article.

Author Disclosure Statement

No competing financial interests exist.

Funding Information

The German Research Foundation (SPP1710; to Katja Becker, Markus Schwarzländer, Stefan Rahlfs, and Holger Gohlke) and LOEWE Center DRUID (Project E3 to Katja Becker and Stefan Rahlfs) supported this study. The German Research Foundation funds the Center for Structural Studies (DFG Grant No. 417919780).

Supplementary Material

Supplementary Information
 Supplementary Figure S1
 Supplementary Figure S2
 Supplementary Figure S3
 Supplementary Figure S4
 Supplementary Figure S5
 Supplementary Figure S6
 Supplementary Table S1

References

- Adams PD, Afonine PV, Bunkoczi G, Chen VB, Davis IW, Echols N, Headd JJ, Hung LW, Kapral GJ, Grosse-Kunstleve RW, McCoy AJ, Moriarty NW, Oeffner R, Read RJ, Richardson DC, Richardson JS, Terwilliger TC, and Zwart PH. PHENIX: a comprehensive Python-based system for macromolecular structure solution. *Acta Crystallogr D Biol Crystallogr* 66: 213–221, 2010.
- Bas DC, Rogers DM, and Jensen JH. Very fast prediction and rationalization of pKa values for protein-ligand complexes. *Proteins* 73: 765–783, 2008.
- Brejč K, Sixma TK, Kitts PA, Kain SR, Tsien RY, Ormö M, and Remington SJ. Structural basis for dual excitation

- and photoisomerization of the *Aequorea victoria* green fluorescent protein. *Proc Natl Acad Sci U S A* 94: 2306–2311, 1997.
- Campbell BC, Petsko GA, and Liu CF. Crystal structure of green fluorescent protein lover and design of clover-based redox sensors. *Structure* 26: 225–237, 2018.
- Case DA, Brozell SR, Cerutti DS, Cheatham TE, Cruzeiro VWD III, Darden TA, Duke RE, Ghoreishi D, Gohlke H, Goetz AW, Greene D, Harris R, Homeyer N, Izadi S, Kovalenko A, Lee TS, LeGrand S, Li P, Lin C, Liu J, Luchko T, Luo R, Mermelstein DJ, Merz KM, Miao Y, Monard G, Nguyen H, Omelyan I, Onufriev A, Pan F, Qi R, Roe DR, Roitberg A, Sagui C, Schott-Verdugo S, Shen J, Simmerling CL, Smith J, Swails J, Walker RC, Wang J, Wei H, Wolf RM, Wu X, Xiao L, York DM, and Kollman PA. *AMBER 2018*. San Francisco: University of California, 2018.
- Chaturvedi D and Mahalakshmi R. Transmembrane β -barrels: evolution, folding and energetics. *Biochim Biophys Acta Biomembr* 1859: 2467–2482, 2017.
- Cormack BP, Valdivia RH, and Falkow S. FACS-optimized mutants of the green fluorescent protein (GFP). *Gene* 173: 33–38, 1996.
- Cramer A, Whitehorn EA, Tate E, and Stemmer WPC. Improved green fluorescent protein by molecular evolution using DNA shuffling. *Nat Biotechnol* 14: 315–319, 1996.
- Dahiyat BI, Gordon DB, and Mayo SL. Automated design of the surface positions of protein helices. *Protein Sci* 6: 1333–1337, 1997.
- Darden T, York D, and Pedersen L. Particle Mesh Ewald: an N.log(N) method for Ewald sums in large systems. *J Chem Phys* 98: 10089–10092, 1993.
- Deller MC, Kong L, and Rupp B. Protein stability: a crystallographer's perspective. *ACTA Crystallogr F* 72: 72–95, 2016.
- Dooley CT, Dore TM, Hanson GT, Jackson WC, Remington SJ, and Tsien RY. Imaging dynamic redox changes in mammalian cells with green fluorescent protein indicators. *J Biol Chem* 279: 22284–22293, 2004.
- Dooley CT, Li L, Mislser JA, and Thompson JH. Toxicity of 6-hydroxydopamine: live cell imaging of cytoplasmic redox flux. *Cell Biol Toxicol* 28: 89–101, 2012.
- Emsley P, Lohkamp B, Scott WG, and Cowtan K. Features and development of Coot. *Acta Crystallogr D Biol Crystallogr* 66: 486–501, 2010.
- Folch B, Rooman M, and Dehouck Y. Thermostability of salt bridges versus hydrophobic interactions in proteins probed by statistical potentials. *J Chem Inf Model* 48: 119–127, 2008.
- Fujita K and Ohno H. Enzymatic activity and thermal stability of metallo proteins in hydrated ionic liquids. *Biopolymers* 93: 1093–1099, 2010.
- Gutscher M, Pauleau AL, Marty L, Brach T, Wabnitz GH, Samstag Y, Meyer AJ, and Dick TP. Real-time imaging of the intracellular glutathione redox potential. *Nat Methods* 5: 553–559, 2008.
- Hanson GT, Aggeler R, Oglesbee D, Cannon M, Capaldi RA, Tsien RY, and Remington SJ. Investigating mitochondrial redox potential with redox-sensitive green fluorescent protein indicators. *J Biol Chem* 279: 13044–13053, 2004.
- Heim R, Prasher DC, and Tsien RY. Wavelength mutations and posttranslational autoxidation of green fluorescent protein. *Biochemistry* 91: 12501–12504, 1994.

20. Hermans SM, Pflieger C, Nutschel C, Hanke CA, and Gohlke H. Rigidity theory for biomolecules: concepts, software, and applications. *Wiley Interdiscip Rev Comput Mol Sci* 7: e1311, 2017.
21. Hesperheide B, Jacobs D, and Thorpe M. Structural rigidity in the capsid assembly of cowpea chlorotic mottle virus. *J Phys Condens Matter* 16: S5055, 2004.
22. Hopkins CW, Le Grand S, Walker RC, and Roitberg AE. Long-time-step molecular dynamics through hydrogen mass repartitioning. *J Chem Theory Comput* 11: 1864–1874, 2015.
23. Ilmberger N, Meske D, Juergensen J, Schulte M, Barthen P, Rabausch U, Angelov A, Mientus M, Liebl W, Schmitz RA, and Streit WR. Metagenomic cellulases highly tolerant towards the presence of ionic liquids—linking thermostability and halotolerance. *Appl Microbiol Biot* 95: 135–146, 2012.
24. Jacobs DJ. Generic rigidity in three-dimensional bonding networks. *J Phys A Math Gen* 31: 6653–6668, 1998.
25. Jacobs DJ, Rader AJ, and Kuhn LA. Protein flexibility predictions using graph theory. *Proteins* 4: 150–165, 2001.
26. Jacobs DJ and Thorpe MF. Generic rigidity percolation: the pebble game. *Phys Rev Lett* 75: 4051, 1995.
27. Jorgensen WL, Chandrasekhar J, Madura JD, Impey RW, and Klein ML. Comparison of simple potential functions for simulating liquid water. *J Chem Phys* 79: 926–935, 1983.
28. Jortzik E and Becker K. Thioredoxin and glutathione systems in *Plasmodium falciparum*. *Int J Med Microbiol* 302: 187–194, 2012.
29. Joung IS and Cheatham TE III. Determination of alkali and halide monovalent ion parameters for use in explicitly solvated biomolecular simulations. *J Phys Chem B* 112: 9020–9041, 2008.
30. Kabsch W. Integration, scaling, space-group assignment and post-refinement. *Acta Crystallogr D Biol Crystallogr* 66: 133–144, 2010.
31. Karshikoff A, Nilsson L, and Ladenstein R. Rigidity versus flexibility: the dilemma of understanding protein thermal stability. *FEBS J* 282: 3899–3917, 2015.
32. Kasozi D, Mohring F, Rahlfs S, Meyer AJ, and Becker K. Real-time imaging of the intracellular glutathione redox potential in the malaria parasite *Plasmodium falciparum*. *PLoS Pathog* 9:e1003782, 2013.
33. Kavishe RA, Koenderik JB, and Alifrangis M. Oxidative stress in malaria and artemisinin combination therapy: pros and cons. *FEBS J* 284: 2579–2591, 2017.
34. Krüger DM, Rathi PC, Pflieger C, and Gohlke H. CNA web server: rigidity theory-based thermal unfolding simulations of proteins for linking structure, (thermo-) stability, and function. *Nucleic Acids Res* 41: W340–W348, 2013.
35. Lakowicz JR, (Ed). *Principles of Fluorescence Spectroscopy*. Boston, MA: Springer Science & Business Media, 2013.
36. LaVallie ER, Lu Z, Diblaso-Smith EA, Collins-Racie LA, and McCoy JM. Thioredoxin as a fusion partner for production of soluble recombinant proteins in *Escherichia coli*. *Methods Enzymol* 326: 322, 2000.
37. Maier JA, Martinez C, Kasavajhala K, Wickstrom L, Hauser KE, and Simmerling C. ff14SB: Improving the accuracy of protein side chain and backbone parameters from ff99SB. *J Chem Theory Comput* 11: 3696–3713, 2015.
38. Mann JP, McCluskey A, and Atkin R. Activity and thermal stability of lysozyme in alkylammonium formate ionic liquids—influence of cation modification. *Green Chem* 11: 785–792, 2009.
39. Meyer AJ and Dick TP. Fluorescent protein-based redox probes. *Antioxid Redox Sign* 13: 621–650, 2010.
40. Minton AP. How can biochemical reaction within cells differ from those in tubes? *J Cell Sci* 119: 2863–2869, 2006.
41. Nakatani T, Yasui N, Tamura I, and Yamahita A. Specific modification at the C-terminal lysine residue of the green fluorescent protein variant, GFPuv, expressed in *Escherichia coli*. *Sci Rep* 9: 1–13, 2019.
42. Naveed H and Liang J. Weakly stable regions and protein-protein interactions in beta-barrel membrane proteins. *Curr Pharm Des* 20: 1268–1273, 2014.
43. Nkrumah LJ, Muhle RA, Moura PA, Ghosh P, Hatfull GF, Jacobs WR, and Fidock DA. Efficient site-specific integration in *Plasmodium falciparum* chromosomes mediated by mycobacteriophage Bxb1 integrase. *Nat Methods* 3: 615–621, 2006.
44. Nutschel C, Fulton A, Zimmermann O, Schwaneberg U, Jaeger K-E, and Gohlke H. Systematically scrutinizing the impact of substitution sites on thermostability and detergent tolerance for *Bacillus subtilis* lipase A. *J Chem Inf Model* 60: 1568–1584, 2020.
45. Pédélecq JD, Cabantous S, Tran T, Terwilliger TC, and Waldo GS. Engineering and characterization of a superfolder green fluorescent protein. *Nat Biotechnol* 24: 79–88, 2006.
46. Pérez VI, Buffenstein R, Masamsetti V, Leonard S, Salmon AB, Mele J, Andziak B, Yang T, Edrey Y, Friguet B, Ward W, Richardson A, and Chaudhuri A. Protein stability and resistance to oxidative stress are determinants of longevity in the longest-living rodent, the naked mole-rat. *Proc Natl Acad Sci U S A* 106: 3059–3064, 2009.
47. Pettersen EF, Goddard TD, Huang CC, Couch GS, Greenblatt DM, Meng EC, and Ferrin TE. UCSF Chimera—a visualization system for exploratory research and analysis. *J Comput Chem* 25: 1605–1612, 2004.
48. Pflieger C and Gohlke H. Efficient and robust analysis of biomacromolecular flexibility using ensembles of network topologies based on fuzzy noncovalent constraints. *Structure* 21: 1725–1734, 2013.
49. Pflieger C, Radestock S, Schmidt E, and Gohlke H. Global and local indices for characterizing biomolecular flexibility and rigidity. *J Comput Chem* 34: 220–233, 2013a.
50. Pflieger C, Rathi PC, Klein DL, Radestock S, and Gohlke H. Constraint Network Analysis (CNA): a Python software package for efficiently linking biomacromolecular structure, flexibility, (thermo-) stability, and function. *J Chem Inf Model* 53: 1007–1015, 2013.
51. Prasher DC, Eckenrode VK, Ward WW, Prendergast FG, and Cormier MJ. Primary structure of the *Aequorea victoria* green-fluorescent protein. *Gene* 111: 229–233, 1992.
52. Privalov PL and Gill SJ. Stability of protein structure and hydrophobic interaction. *Adv Protein Chem* 39: 191–234, 1988.
53. Radestock S and Gohlke H. Exploiting the link between protein rigidity and thermostability for data-driven protein engineering. *Eng Life Sci* 8: 507–522, 2008.
54. Radestock S and Gohlke H. Protein rigidity and thermophilic adaptation. *Proteins* 79: 1089–1108, 2011.

55. Rathi PC, Fulton A, Jaeger K-E, and Gohlke H. Application of rigidity theory to the thermostabilization of lipase A from *Bacillus subtilis*. *PLoS Comput Biol* 12: e1004754, 2016.
56. Rathi PC, Jaeger K-E, and Gohlke H. Structural rigidity and protein thermostability in variants of lipase A from *Bacillus subtilis*. *PLoS One* 10: e0130289, 2015a.
57. Rathi PC, Mulnaes D, and Gohlke H. VisualCNA: a GUI for interactive constraint network analysis and protein engineering for improving thermostability. *Bioinformatics* 31: 2394–2396, 2015.
58. Rathi PC, Radestock S, and Gohlke H. Thermostabilizing mutations preferentially occur at structural weak spots with a high mutation ratio. *J Biotechnol* 159: 135–144, 2012.
59. Rivas G and Minton AP. Macromolecular crowding in vitro, in vivo, an in between. *Trends Biochem Sci* 41: 970–981, 2016.
60. Roe DR and Cheatham TE III. Parallelization of CPPTRAJ enables large scale analysis of molecular dynamics trajectory data. *J Comput Chem* 39: 2110–2117, 2018.
61. Roe DR and Cheatham TE III. PTRAJ and CPPTRAJ: software for processing and analysis of molecular dynamics trajectory data. *J Chem Theory Comput* 9: 3084–3095, 2013.
62. Ryckaert JP, Ciccotti G, and Berendsen HJC. Numerical-integration of Cartesian equations of motion of a system with constraints—molecular-dynamics of N-alkanes. *J Comput Phys* 23: 327–341, 1977.
63. Schindelin J, Arganda-Carreras I, Frise E, Kaynig V, Longair M, Pietzsch T, Preibisch S, Rueden C, Saalfeld S, Schmid B, Tinevez J-Y, White DJ, Hartenstein V, Eliceiri K, Tomancak P, and Cardona A. Fiji: an open-source platform for biological-image analysis. *Nat Methods* 9: 676–682, 2012.
64. Schuh AK, Rahbari M, Heimsch KC, Mohring F, Gabryszewski SJ, Weder S, Buchholz K, Rahlfs S, Fidock DA, and Becker K. Stable integration and comparison of hGrx1-roGFP2 and sfroGFP2 redox probes in the malaria parasite *Plasmodium falciparum*. *ACS Infect Dis* 4: 1601–1612, 2018.
65. Schwarzländer M, Dick TP, Meyer AJ, and Morgan B. Dissecting redox biology using fluorescent protein sensors. *Antioxid Redox Signal* 24: 680–712, 2016.
66. Shimomura O. Structure of the chromophore of *Aequorea* green fluorescent protein. *FEBS Lett* 104: 220–222, 1979.
67. Shimomura O, Johnson FH, and Saiga Y. Extraction, purification and properties of aequorin, a bioluminescent protein from the luminous hydromedusa, *Aequorea*. *J Cell Comp Physiol* 59: 223–239, 1962.
68. This reference has been deleted.
69. Trager W and Jensen JB. Human malaria parasites in continuous culture. *Science* 193: 673–675, 1976.
70. Waldo GS, Standish BM, Berendzen J, and Terwilliger TC. Rapid protein-folding assay using green fluorescent protein. *Nat Biotechnol* 17: 691–695, 1999.
71. Wang J, Wang W, Kollman PA, and Case DA. Antechamber: an accessory software package for molecular mechanical calculations. *J Am Chem Soc* 222: U403, 2001.
72. Waterhouse A, Bertoni M, Bienert S, Studer G, Tauriello G, Gumienny R, Heer FT, de Beer TAP, Rempfer C, Bordoli L, Lepore R, and Schwede T. SWISS-MODEL: homology modelling of protein structures and complexes. *Nucleic Acids Res* 46: 296–303, 2018.
73. Whiteley W. Counting out to the flexibility of molecules. *Phys Biol* 2: S116, 2005.

Address correspondence to:

Dr. Karin Fritz-Wolf

Biochemistry and Molecular Biology

Interdisciplinary Research Center

Justus Liebig University Giessen

Giessen 35392

Germany

E-mail: karin.fritz@mr.mpg.de

Date of first submission to ARS Central, October 26, 2021; date of final revised submission, December 7, 2021; date of acceptance, January 6, 2022.

Abbreviations Used

λ_{iso}	= isosbestic point
AA	= amino acid
AB	= antibody
ASU	= asymmetric unit
avGFP	= <i>Aequorea victoria</i> GFP
CNA	= constraint network analysis
Cn ^R	= carbenicillin resistance
CRO	= chromophore
DIA	= diamide
DPS	= 2,2-dithiopyridylsulfide
DTT	= dithiothreitol
DTT _{ox}	= 1,3-dithiane
DTT _{red}	= 1,4-dithiothreitol
FI	= fluorescence intensity
GFP	= green fluorescent protein
Grx1	= glutaredoxin-1
hGrx1-roGFP2	= human glutaredoxin-1 fused to reduction/oxidation-sensitive green fluorescent protein
hGrx1-sfroGFP2	= human glutaredoxin-1 fused to superfolder reduction/oxidation-sensitive green fluorescent protein
HRP	= horseradish peroxidase
Kan ^R	= kanamycin resistance
LB	= lysogeny broth
MD	= molecular dynamics
NVT	= constant number of particles, volume, and temperature
OxD	= degree of oxidation
PDB	= Protein Data Bank
PEG	= polyethylene glycol
RFU	= random fluorescence intensity units
RMSZ	= the root mean square of all zscores of the bond lengths (or angles)
roGFP2	= reduction/oxidation-sensitive green fluorescent protein
RT	= room temperature
SDS-PAGE	= sodium dodecyl sulfate–polyacrylamide gel electrophoresis
sf	= superfolder
sfroGFP2	= superfolder reduction/oxidation-sensitive green fluorescent protein
WT	= wild type